The Astrophysical Journal, 656:847–869, 2007 February 20


# THE ORIGIN OF DIFFUSE X-RAY AND $\gamma$-RAY EMISSION FROM THE GALACTIC CENTER REGION: COSMIC-RAY PARTICLES

F. Yusef-Zadeh,[1] M. Muno,[2] M. Wardle,[3] and D. C. Lis[4]

*Received 2006 August 23; accepted 2006 November 6*


## ABSTRACT

The inner couple of hundred parsecs of our Galaxy are characterized by a significant amount of synchrotron-emitting gas. Many of the best studied sources in this region exhibit a mixture of 6.4 keV Fe K$\alpha$ emission, molecular line emission, and nonthermal radio continuum radiation. The spatial correlation between fluorescent Fe K$\alpha$ line emission at 6.4 keV and molecular line emission from Galactic center molecular clouds has been explained as reflected X-rays from a past outburst of Sgr A$^*$. Here we present a multiwavelength study of this region and find a correlation between the nonthermal radio filaments and the X-ray features. This correlation, when combined with the distribution of molecular gas, suggests against the irradiation model. Instead, we account for this distribution in terms of the impact of the relativistic particles from local (nonthermal filaments) and extended sources with diffuse neutral gas producing both nonthermal bremsstrahlung X-ray continuum emission and diffuse 6.4 keV line emission. The production rate of Fe K$\alpha$ photons associated with the injection of electrons into a cloud as a function of column density is calculated. The required energy density of low-energy cosmic rays associated with the synchrotron-emitting radio filaments or extended features is estimated to be in the range between 20 and $\sim 10^3$ eV cm$^{-3}$ for Sgr C, Sgr B1, Sgr B2, and "the 45 and $-30$ km s$^{-1}$" clouds. We also generalize this idea to explain the cosmic-ray heating of molecular gas, the interstellar cosmic-ray ionization, the pervasive production of the diffuse K$\alpha$ line, and TeV emission from the Galactic center molecular clouds. In particular, we suggest that inverse Compton scattering of the submillimeter radiation from dust by relativistic electrons may contribute substantially to the large-scale diffuse TeV emission observed toward the central regions of the Galaxy.


*Subject headings:* cosmic rays — Galaxy: center — H II regions — ISM: general — X-rays: ISM

## 1. INTRODUCTION

It is well recognized that the Galactic center region hosts several sources of energetic activity in the form of nonthermal linear filaments, supernova remnants, and colliding winds of massive stars. This region is also recognized to be the site of massive molecular clouds with pockets of ongoing and past massive star formation. The most prominent of these clouds are associated with Sgr B2, Sgr C, and the clouds associated with the radio continuum arc and Sgr A. Sgr C or G359.43$-$0.09 is one of the best examples of a massive star-forming region that hosts prominent thermal and nonthermal radio continuum, millimeter, submillimeter, and X-ray sources in the Galactic center region. This massive star-forming region is identified by its H II region, a dense molecular cloud, and nonthermal radio filaments. This source is also known as an X-ray source based on *ASCA* observations (Murakami et al. 2001b), showing evidence of iron K-shell fluorescence (K$\alpha$) line emission. To probe the nature of high-energy activity in the Galactic center region, we have selected to study Sgr C in detail, as well as star-forming regions near the continuum arc ($l \sim 0.2^\circ$) and the Sgr B complex.

Sgr C consists of a thermal radio continuum, a far-IR and a submillimeter source, and a synchrotron-emitting source associated with magnetized filaments (Odenwald & Fazio 1984; Caswell & Haynes 1987; Liszt 1992; Tsuboi et al. 1991; Lis & Carlstrom 1994). The Sgr C H II complex is thought to be powered by a single O4 zero-age main-sequence (ZAMS) star. The molecular mass of Sgr C is estimated to be $\sim(5–6) \times 10^5\ M_\odot$ with column density of $N_{\rm H_2} \sim 10^{23}$ cm$^{-2}$, based on submillimeter and $^{13}$CO observations (Liszt & Spiker 1995; Lis & Carlstrom 1994). A recent radio continuum survey of the Galactic center region has identified additional nonthermal filaments distributed in the immediate vicinity of the Sgr C H II region (Nord et al. 2004; Yusef-Zadeh et al. 2004). The main nonthermal radio filament (NRF) appears to end abruptly inside the Sgr C molecular H II complex M359.5$-$0.15 with a velocity of $-65$ km s$^{-1}$ (Liszt & Spiker 1995). Similar radio recombination line velocity has also been detected from the Sgr C H II region (Anantharamaiah & Yusef-Zadeh 1989). H I absorption measurements toward the nonthermal filament and the H II region constrain the distance to both sources within the inner 200 pc of the Galactic center. However, Roy (2003) suggests that the Sgr C filament and H II region are two separate objects and may not be interacting with each other (Roy 2003).

The *ASCA* measurements show the presence of strong fluorescent 6.4 keV line emission from neutral iron gas implying $H_2$ column density similar to that of molecular line observations (Murakami et al. 2001b). The nature of the 6.4 keV line emission has been considered to be due to the irradiation of the Sgr C molecular cloud originated by past energetic outburst from Sgr A$^*$ (Murakami et al. 2001b). A similar mechanism has been postulated to explain the origin of the strong 6.4 keV line emission detected from other Galactic center molecular clouds (e.g., Sgr B2) either by Sgr A$^*$ or from the interaction of Sgr A East and "the 50 km s$^{-1}$ cloud" (Koyama et al. 1996; Murakami et al. 2000, 2001a; Revnivtsev et al. 2004; Fryer et al. 2006). An alternative explanation to the X-ray reflection nebula model has

[1] Department of Physics and Astronomy, Northwestern University, Evanston, IL; zadeh@northwestern.edu.
[2] Department Physics and Astronomy, UCLA, Los Angeles, CA; mmuno@astro.ucla.edu.
[3] Department of Physics, Macquarie University, Sydney, Australia; wardle@physics.mq.edu.au.
[4] California Institute of Technology, Pasadena, CA; dcl@caltech.edu.

accounted for the origin of X-ray emission in terms of the impact of low-energy cosmic-ray (LECR) particles with neutral gas associated with the M0.11−0.08 molecular cloud (Yusef-Zadeh et al. 2002). These authors speculated that the same process could also explain the origin of the 6.4 keV line emission from other Galactic center molecular clouds.

The structure of this paper is as follows. In § 2 we reanalyze the archival *Chandra* observations of the Galactic center region followed by the analysis of new millimeter line and radio continuum data using FCRAO and the Very Large Array (VLA). In § 3 we report the discovery of X-ray filamentary structures in Sgr C. The morphology of X-ray and nonthermal radio continuum features suggests that many of the K$\alpha$ 6.4 keV line features lie near the nonthermal radio filaments at 20 and 90 cm wavelengths. We also examine the morphology of $^{13}$CO and Fe K$\alpha$ lines and estimate column densities using millimeter and X-ray techniques. We present spectral index determination in § 3.1.5 and polarization measurements of the brightest filament in Sgr C at radio wavelengths in the Appendix. The synchrotron parameters of the Sgr C filament are critical in support of our picture that the low-energy component of the synchrotron-emitting particles penetrates molecular clouds. We then compare the distribution of 6.4 keV and TeV emission from prominent Galactic center molecular clouds. The overall correlations of K$\alpha$ line emission, molecular line emission from the "45 and −30 km s$^{-1}$ clouds," TeV emission, and nonthermal radio continuum features are described. In § 4 we argue in support of enhanced cosmic rays in the central region of the Galaxy and compare the irradiation model versus the LECR model to account for the origin of the 6.4 keV emission. We then describe a quantitative mode of injection of cosmic rays into molecular clouds and the subsequent heating of gas before this model is applied to the Galactic center molecular clouds. Unlike the irradiation model, the picture that is presented here can naturally explain the high temperature of molecular gas in the Galactic center region. Lastly, we investigate the origin of diffuse TeV emission from Galactic center clouds in terms of the inverse Compton scattering of dust emission by the high-energy component of the cosmic rays distributed throughout this unique region of the Galaxy.

## 2. DATA REDUCTIONS

### 2.1. *X-Ray Analysis*

Sgr C was observed with the *Chandra* Advanced CCD Imaging Spectrometer (ACIS-I; Weisskopf et al. 2002) as part of the shallow Galactic center survey (Wang et al. 2002) with two overlapping 11 ks exposures on 2001 July 20 (sequences 2270 and 2272). We reduced the observation using standard tools that are part of CIAO version 3.2. We first created a cleaned event list from the ACIS-I array for each observation. We corrected the pulse heights of the events for position-dependent charge transfer inefficiency (Townsley et al. 2002) and excluded events that did not pass the standard *ASCA* grade filters and *Chandra* X-Ray Center (CXC) good-time filters. We searched for intervals during which the background rate flared to $\geq 3\ \sigma$ above the mean level and found none. Our goal was to study the properties of diffuse features, so we removed events within circles enclosing at least 92% of the point-spread function that were centered at the locations of the pointlike X-ray sources, as identified by Muno et al. (2006). Finally, we reprojected the events from each observation onto a fixed tangent point (the location of Sgr A$^*$), so that they could be combined to form composite images.

We then generated images of the continuum emission between 4 and 8 keV, excluding the 6.10–7.15 keV energy range containing iron lines, with a resolution of 9″. In addition to the continuum images, we also made the Fe K$\alpha$ flux and equivalent width images. Both the continuum and line flux images were made the same way. For display purposes, the holes left in the image when we excluded point sources were filled with pixel values drawn from a Poisson distribution that had the mean value of the pixels in a surrounding annulus. We repeated the same process on an image of an exposure image generated with standard CIAO tools and then divided the count image by the resulting exposure image in order to create a flux image of the diffuse emission. Finally, we present two different types of images, one of which is adaptively smoothed using the CIAO tool `csmooth`, whereas the other is convolved with 30″ Gaussians.

Images of the equivalent widths of the low-ionization 6.4 keV line of Fe were constructed using the techniques described by Park et al. (2004). Adaptively smoothed images of the diffuse line emission were generated in the same manner as the continuum image, using the 6.25–6.50 keV band for Fe K$\alpha$. The continuum under each line was computed based on adaptively smoothed images of the flux in the 5.0–6.1 keV and 7.15–7.30 keV energy bands. We assumed that the flux in each continuum band ($F_{\rm band}$) could be described as a power law, so that the normalization ($N$) and slope ($\Gamma$) of the power law could be computed from

$$F_{\rm band} = \frac{NE_{\rm low}^{-\Gamma+1} - NE_{\rm high}^{-\Gamma+1}}{\Gamma - 1}. \quad (1)$$

Using the fluxes in both continuum bands, the above equation was solved for $N$ and $\Gamma$ using Newton's algorithm, and the parameters were used to estimate the continuum contribution to the line emission images. To derive the equivalent width images, we subtracted the estimated total continuum flux from the line image and then divided the line image by the continuum flux density at the centroid of the line (6.4 keV). We caution that we have neglected the cosmic-ray background in generating these maps, which could account for as much as ∼40% of the events in the 6–7 keV band and consequently biases any estimate of the equivalent width. The assumption of a power-law spectrum also introduces a small systematic bias in these maps. We have not attempted to correct these effects because they are only used to search for regions of enhanced iron emission.

In order to confirm the properties suggested by the images of the diffuse line and continuum emission, we examined the spectra of small regions of the image. For each observation, counts were extracted from each region of interest and then binned as a function of pulse height to create spectra. We obtained the response functions from Townsley et al. (2002) and averaged them weighted by the number of counts received by the relevant portions of the detectors. Effective area functions for the spectra of each observation were generated using `mkwarf` and averaged weighted by the counts in each observation. The background was estimated from the spectrum of the particles that impacted the detectors during a 50 ks observation taken with the ACIS-I stowed out of the focal plane of the mirror assembly.

### 2.2. *Millimeter Line Analysis*

The $^{13}$CO (1–0) data presented here were taken in 1993 April using the 15-element QUARRY focal plane array mounted at the Cassegrain focus of the 14 m FCRAO telescope. Each pixel of the receiver employed a cooled Schottky diode mixer and 1.3–1.7 GHz HEMT IF amplifier. There was a common quasi-optical single sideband filter with cooled image termination (Erickson et al. 1992). The back end was a wideband filter bank spectrometer

having 32 channels with 5 MHz (13.6 km s$^{-1}$) resolution for each pixel of the array. Typical system temperatures referred to above the Earth's atmosphere were ~800–1200 K, the FWHM beam size was ~50″, and the main-beam efficiency was ~40%. The $^{13}$CO spectra were taken at 720 positions, with approximately one beam spacing, covering an area of $25' \times 20'$. The raw data were converted to CLASS format and the subsequent data reduction and analysis were carried out using the IRAM GILDAS software package.

### 2.3. *Radio Continuum Analysis*

The 20 cm images presented here are based on observations with the VLA of the National Radio Astronomy Observatory[5] that were carried out using B, C, and D configurations. Details of data reductions are described in Yusef-Zadeh et al. (2004). To measure the spectral index distribution, we compared the 20 cm image with a 90 cm image that was also based on multiconfiguration observations with the VLA (Nord et al. 2004). The spatial frequency coverages of both the 20 and 90 cm data were similar to each other so an accurate spectral index distribution could be determined. We convolved both images to a Gaussian having an FWHM $= 12.6'' \times 12.6''$ before the spectral index image was constructed in AIPS. The rms noise for the two images is 3.6 and 2.5 mJy beam$^{-1}$ at 90 and 20 cm, respectively.

To search for polarized emission from Sgr C, we also reduced radio continuum observations of Sgr C at 3.6 and 2 cm that were observed in the DnC hybrid array configuration of the VLA on 1988 June 19. Standard calibration was done using NRAO 530 and 3C 286 as the phase and flux calibrators, respectively. The phase center for both pointings at 3.6 and 2 cm wavelengths is centered at $l = 359^\circ 27' 14.04''$, $b = -2' 10.3''$. Based on 3.6 and 2 cm, we also placed a limit on the spectral index of the nonthermal filaments in Sgr C.

## 3. RESULTS

We have compared the spatial distribution of X-ray, nonthermal radio continuum, molecular line, and TeV emission and find a rough correspondence that suggests that they are related to each other. In particular, the analysis of the diffuse X-ray, molecular line, and nonthermal radio continuum emission derives the iron flux, the column depth of molecular gas, and the nonthermal particle flux. These basic observables are then used to measure how cosmic rays interact with neutral material.

### 3.1. *The Sgr C Molecular Complex*

#### 3.1.1. *Diffuse X-Ray Emission*

Figure 1*a* shows contours of X-ray continuum emission from Sgr C between 2 and 6 keV. We note the evidence for several extended X-ray features in this H II complex. Diffuse features run vertically perpendicular to the Galactic plane, one of which is G359.42−0.12 with an extent of about >4′ running to the south, and the other is G359.45−0.07 with similar extent but appearing clumpy as it runs to the north. Three relatively isolated and compact features are also found near G359.45−0.07, G359.32−0.16, and G359.46−0.15 with an extent of ~1′. These individual X-ray features are discussed in §§ 3.1.2 and 3.1.4.

We extracted an average X-ray spectrum of Sgr C from a region that enclosed the brightest parts of the diffuse and compact emission, as noted in Figure 1*a*, in the smoothed line images. We accounted for the background using the particle spectrum before we made the X-ray spectrum, as shown in Figure 1*b*. The extracted region is shown as an ellipse in a gray-scale 6.4 keV EW image in Figure 2. The resulting spectrum of Sgr C looks very similar to that of the diffuse emission analyzed by Muno et al. (2004a). The emission spectrum was modeled with a two-temperature plasma

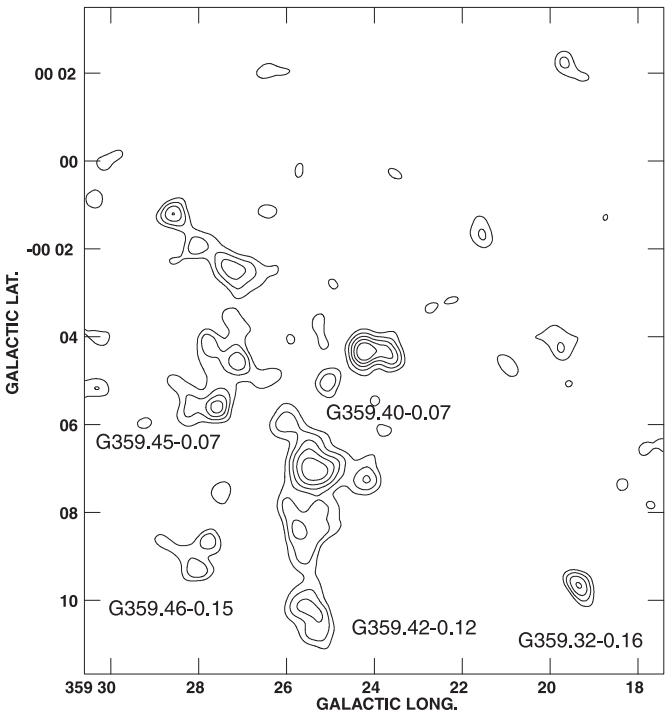


FIG. 1*a*

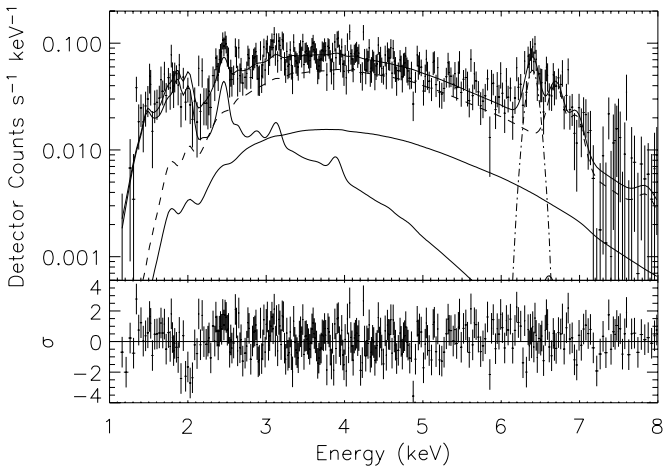


FIG. 1*b*

FIG. 1.—(*a*) Contours of X-ray continuum emission between 2 and 6 keV. The X-ray data are convolved with a Gaussian beam having FWHM ~ 30″. Contour levels are set at $(7, 8, 9, 10, 11) \times 10^{-9}$ Jy beam$^{-1}$. The diffuse and compact X-ray continuum features are labeled. (*b*) Modeling of the X-ray spectrum of diffuse emission from Sgr C and the corresponding residuals in the bottom panel. The thick solid line is the model, the dashed and thin solid lines correspond to the 5 and 1 keV plasma components, the dot-dashed line is the emission line from low-ionization iron, and the triple-dot–dashed line is the power law. The residuals are in units of the 1 $\sigma$ uncertainty on the spectrum. As shown in Fig. 2, the spectrum was taken from an ellipse centered on $l = 359.43382^\circ$, $b = -0.09655^\circ$ with radii of 4.1′ and 2.9′ along the *l*- and *b*-directions, respectively (P.A. = 28.6°).

[5] The National Radio Astronomy Observatory is a facility of the National Science Foundation, operated under a cooperative agreement by Associated Universities, Inc.

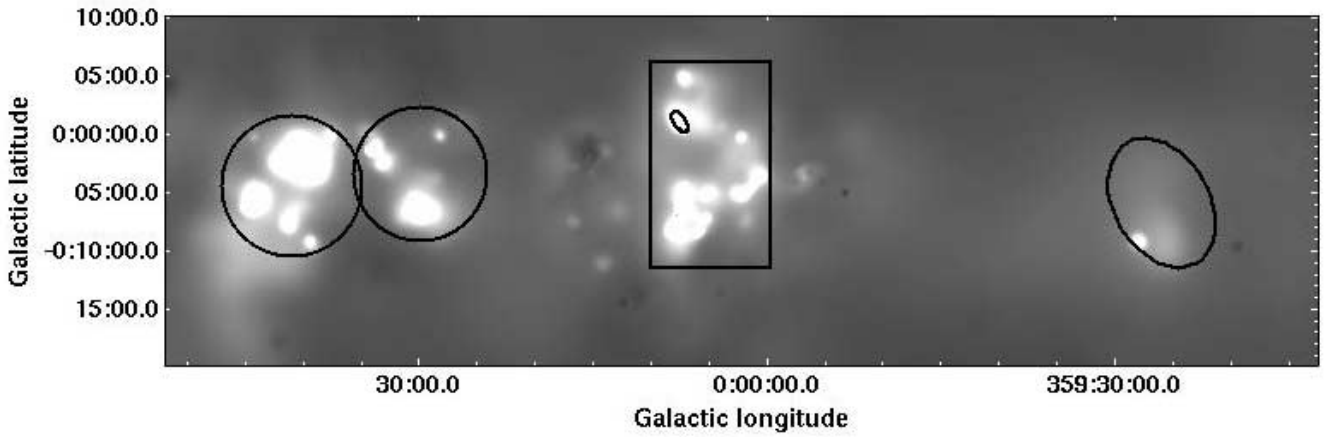


FIG. 2.—Distribution of K$\alpha$ 6.4 keV EW line emission. The regions from which X-ray spectra are extracted are drawn as an ellipse (Sgr C, the Arches cluster), a rectangle (the arc), and circles (Sgr B1 and Sgr B2).

with and without a power-law component using the XSPEC spectral modeling package (Arnaud 1996). We assumed that each component was in collisional ionization equilibrium (the APEC model in XSPEC), although the two components were not physically coupled (e.g., by conduction). We assumed that both components were absorbed by the same interstellar gas and dust, which we took to be distributed nonuniformly along the line of sight and across the image such that its effect could be described mathematically as

$$e^{-\sigma(E)N_{\rm H}}\left[(1-f)+fe^{-\sigma(E)N_{\rm pc,H}}\right]. \quad (2)$$

Here $\sigma(E)$ is the energy-dependent absorption cross section, $N_{\rm H}$ is the absorption column affecting the entire plasma, $N_{\rm pc,H}$ is the column affecting part of the column, and $f$ is the fraction of the plasma affected by $N_{\rm pc,H}$. The parameters of the best-fit model are listed in Table 1.

TABLE 1
SPECTRUM OF THE DIFFUSE X-RAY EMISSION FROM Sgr C

| Parameter | Value |
|---|---|
| $N_{\rm H,1}$ ($10^{22}$ cm$^{-2}$) | $4.0^{+0.3}_{-0.1}$ |
| $N_{\rm H,pc,1}$ ($10^{22}$ cm$^{-2}$) | $10.7^{+0.5}_{-0.7}$ |
| $f_{\rm pc,1}$ | >0.97[a] |
| $kT_1$ (keV) | 0.5 ± 0.1 |
| $Z_1$ | 0.3 ± 0.1 |
| $K_{\rm em,1}$ (cm$^{-6}$ pc) | $231.5^{+79.2}_{-70.7}$ |
| $kT_2$ (keV) | $7.6^{+1.0}_{-0.8}$ |
| $Z_2$ | 0.6 ± 0.1 |
| $K_{\rm em,2}$ (cm$^{-6}$ pc) | 1.0 ± 0.1 |
| $F_{\rm Fe\,K\alpha}$ ($10^{-7}$ photons cm$^{-2}$ s$^{-1}$ arcmin$^{-1}$) | 12 ± 1 |
| $\chi^2/\nu$ | 335/325 |
| $F_{{\rm X},s}$ ($10^{-14}$ ergs cm$^{-2}$ s$^{-1}$ arcmin$^{-2}$) | 3 |
| $F_{{\rm X},h}$ ($10^{-14}$ ergs cm$^{-2}$ s$^{-1}$ arcmin$^{-2}$) | 9 |
| $L_{{\rm X},s}$ ($10^{33}$ ergs s$^{-1}$ arcmin$^{-2}$) | 3 |
| $L_{{\rm X},h}$ ($10^{33}$ ergs s$^{-1}$ arcmin$^{-2}$) | 2 |

NOTES.—Uncertainties are 1 $\sigma$, computed using $\Delta\chi^2 = 1.0$. The emission measure is defined as $K_{\rm em} = \int n_e n_{\rm H}\, dl$, where $dl$ is the integral over the length in parsecs. Fluxes are observed values in the 2–8 keV band, and luminosities are computed from the dereddened flux in the 2–8 keV band. The soft component emits <1% of its flux in the 2–8 keV band, so its emission measure could be lower by a factor of ≈100 if it is produced in a region with a lower column density than the hard emission.

[a] Parameter was not allowed to vary.

The spectrum of the X-ray emission from Sgr C resembles that toward the inner 20 pc of the Galaxy, in that it can be modeled as plasma components with $kT_s \approx 0.5$ and $kT_h \approx 8$ keV (Muno et al. 2004a). It is highly absorbed, with the column density toward >97% of the region reaching $10^{23}$ cm$^{-2}$, which is comparable to the total column depth of the molecular cloud. The derived emission measure of the soft plasma, $\int n_e n_{\rm H}\, dl$ (Table 1), is highly dependent on the absorption column because a ≈0.5 keV plasma emits <1% of its flux in the 2–8 keV band and photons below 2 keV are absorbed by the interstellar medium (ISM). Therefore, there is a factor of ∼100 systematic uncertainty in the emission measure of the soft plasma, and our results cannot be compared easily to those using different absorption models. The emission measure of the hard plasma is less affected by absorption. We find a value of 1.0 ± 0.1 cm$^{-6}$ pc toward Sgr C, which is only a factor of 2 less than the average value of the inner 20 pc of the Galaxy (Muno et al. 2004a).[6] Likewise, the intensity of the Fe K$\alpha$ emission toward Sgr C is similar to that in the central 20 pc of the Galaxy, $\sim(1.2 \pm 0.1) \times 10^{-6}$ photons cm$^{-2}$ s$^{-1}$ arcmin$^{-2}$. The equivalent width of the Fe K$\alpha$ line is 460 ± 100 eV.

In the case where the spectrum was modeled by the inclusion of a power-law component, the fit is no better with a power law than without one. If we assume that the hot plasma producing the 6.7 keV iron lines has solar abundance, then up to 20% of the total deabsorbed 2–8 keV flux could be produced by a power law with the photon index $\Gamma$ between 1 and 2. If we assume that the plasma has twice-solar iron abundance, then up to 45% of the flux could be produced by a nonthermal plasma. If larger abundances are assumed, as some Galactic center diffuse features such as the Arches and Quintuplet clusters indicate (e.g., Yusef-Zadeh et al. 2002; Law & Yusef-Zadeh 2004; Wang et al. 2006), it would imply that the line emission is accompanied by very little thermal continuum, so that the power law can contribute yet more to the spectrum.

#### 3.1.2. *X-Ray and* 20 cm *Continuum Emission*

Figures 3*a* and 3*b* show contours of X-ray continuum emission between 2 and 6 keV superimposed on two gray-scale renditions of continuum emission from Sgr C at 20 cm. The 20 cm image shows the circular Sgr C H II region, as well as the prominent vertical structure that consists of bright nonthermal filaments

[6] We note that in Table 3 of Muno et al. (2004a) the emission measure is erroneously listed as being in units of $10^{-4}$ cm$^{-6}$ pc. It should actually be cm$^{-6}$ pc, as in Table 1 of this paper.

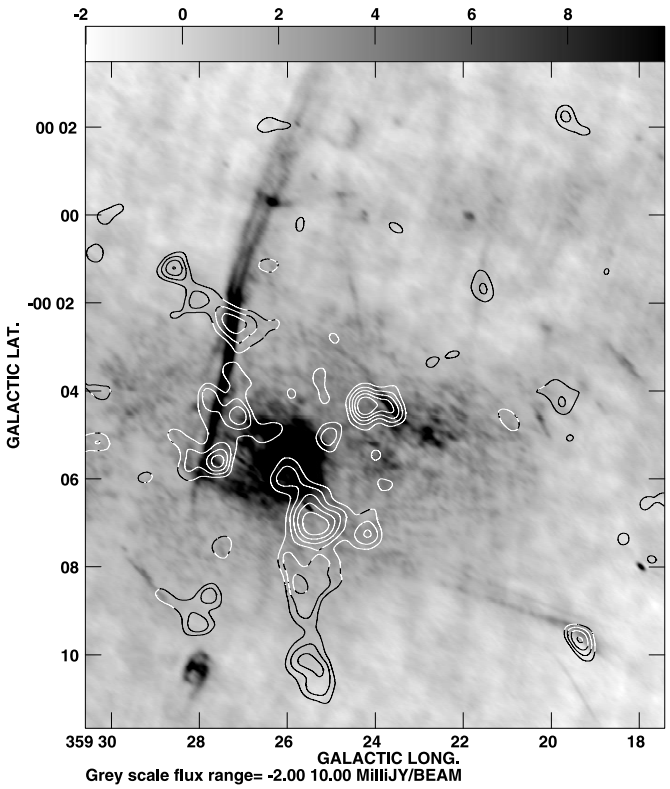


FIG. 3*a*

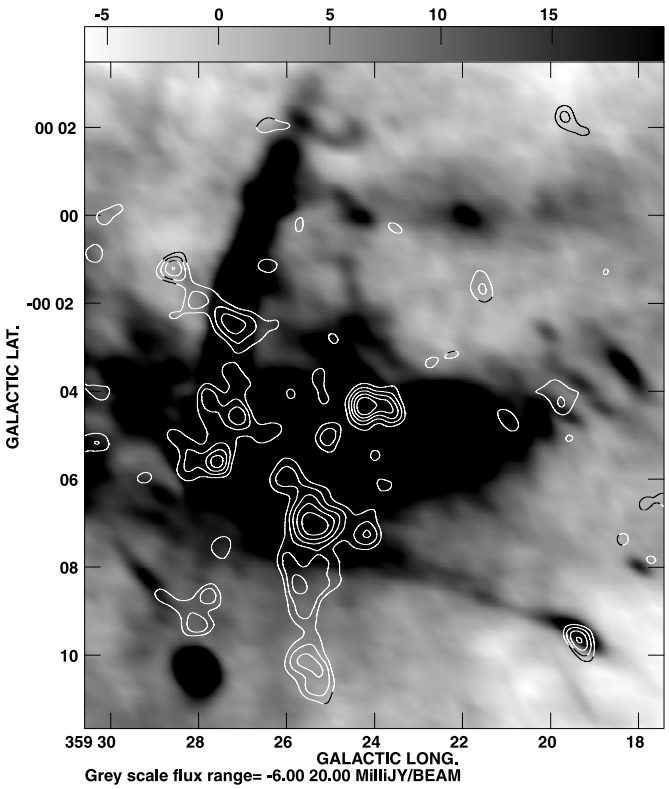


FIG. 3*b*

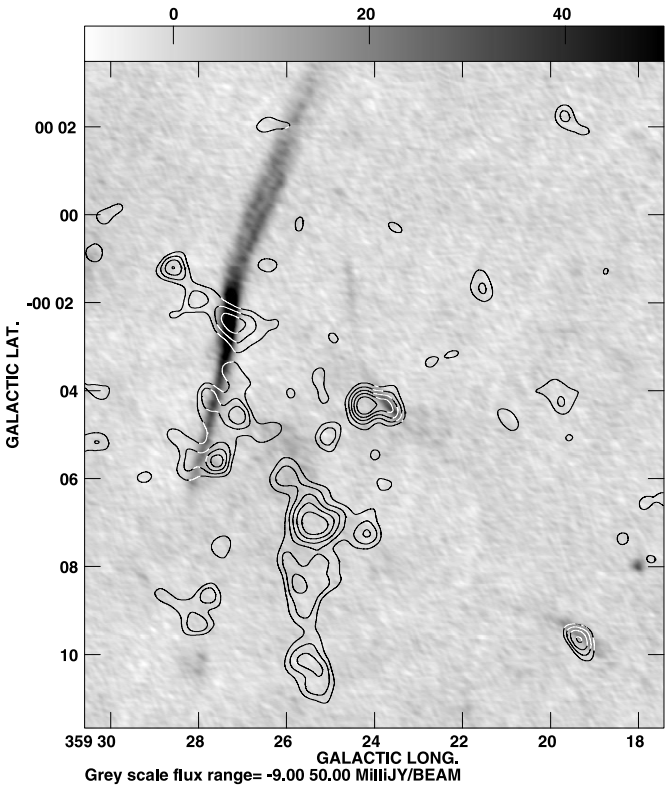


FIG. 3*c*

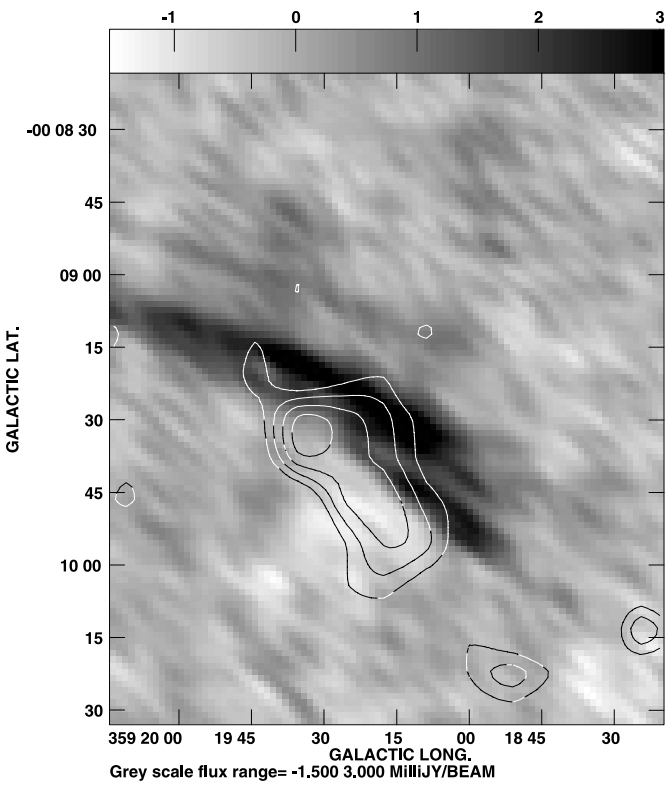


FIG. 3*d*

FIG. 3.—(*a*) Contours of X-ray emission between 2 and 6 keV superimposed on a 20 cm continuum image with a resolution of $9.8'' \times 4.2''$ (P.A. $= -12^\circ$). The contour levels are set at (7, 8, 9, 10, 11) $\times 10^{-9}$ Jy. The X-ray data are convolved by a Gaussian having FWHM = 30 arcsec$^2$. (*b*) Contours of X-ray emission are the same as in (*a*). The surface brightness of a 20 cm continuum image with a resolution of 30 arcsec$^2$ ranges between $-9$ and 200 mJy beam$^{-1}$ in order to bring out the faint features. (*c*) Contours of X-ray emission are the same as in (*a*). The surface brightness of a 90 cm continuum image with a resolution of $12.6'' \times 6.8''$ (P.A. $= 3^\circ$) is taken from Nord et al. (2004). (*d*) Close-up view of G359.32$-$0.1 with contours of X-ray emission superimposed on a 20 cm continuum image (in gray scale) with a spatial resolution of $8.1'' \times 3.3''$ (P.A. $= -11^\circ$). The contour levels are set at 0.8, 1, 1.2, and 1.4 nJy. The X-ray image is convolved to a $9''$ Gaussian.

running vertically toward more positive latitudes in the direction away from the Galactic plane. Figure 3*c* shows the same contours superimposed on a 90 cm image of the Sgr C region to present the relative distribution of nonthermal continuum and X-ray emission. Due to their steep spectrum, 90 cm continuum emission is generally a good tracer of nonthermal emission from synchrotron sources (Nord et al. 2004). We describe individual nonthermal radio filaments and argue that each radio filament has X-ray correspondence. The peaks of radio and X-ray features appear to be displaced between 15″ and 60″ with respect to each other. Five X-ray features are labeled in Figure 1*a*, all of which appear to be spatially correlated with the nonthermal radio continuum features, as described below:

1. *G359.45−0.07*.—One of the diffuse but clumpy X-ray features, G359.45−0.07, as labeled in Figure 1*a*, runs along the brightest portion of the nonthermal radio filament of Sgr C. This nonthermal radio counterpart, labeled as RF-C1 (G359.45−0.06) in Yusef-Zadeh et al. (2004), is prominently detected at 90 cm (Nord et al. 2004).
2. *G359.42−0.12*.—Another X-ray feature that appears to have a radio correspondence is G359.42−0.12, running parallel to a new vertical radio continuum feature. This new faint radio feature, as noted best in Figure 3*b*, extends for 8′ with a typical surface brightness of ∼10 mJy beam$^{-1}$. This radio continuum feature at $l = 359^{\circ}26'$ runs parallel to the eastern edge of the elongated X-ray feature G359.42−0.12. The centroid of the radio continuum and the X-ray continuum features is displaced by ∼1′ in the east-west direction.
3. *G359.40−0.07*.—The third X-ray feature that appears to have a radio correspondence is G359.40−0.007 (Figs. 3*a* and 3*c*). This X-ray feature lies at the northeastern edge of a filamentary radio feature that has been identified earlier at 20 cm (see RF-C14 [G359.32−0.06] in Yusef-Zadeh et al. 2004) and at 90 cm (Nord et al. 2004).
4. *G359.46−0.15*.—Another X-ray feature G359.46−0.15 is noted at the southwestern edge of a long filamentary structure identified as RF-C4 (G359.49−0.12) at 20 cm (Yusef-Zadeh et al. 2004). Figure 3*b* shows the relative location of this faint X-ray emission with respect to the filament. An H II region (G359.47−0.17) lies to the south of the X-ray feature.
5. *G359.32−0.16*.—Lastly, we notice in Figures 3*a*–3*c* a compact X-ray feature G359.32−0.16, which coincides with the brightest component of a nonthermal radio filament. This filament runs diagonally with a position angle of ∼60° and is identified at 20 cm as RF-C13 in Yusef-Zadeh et al. (2004) and at 90 cm (Nord et al. 2004). High-resolution radio continuum images show that the radio filament consists of multiple linear components running parallel to each other but peaking at the location of the X-ray feature G359.32−0.16. Figure 3*d* shows a close-up view of G359.32−0.16 where contours of X-ray emission are superimposed on a gray-scale 20 cm continuum image. The distribution of X-ray emission is elongated along the direction of two parallel nonthermal radio filaments, suggesting that the X-ray and radio features could be associated with each other. Like other X-ray features that have radio continuum correspondence, a displacement of ∼15″ is noted between the peaks of X-ray and radio emission. The displacement between nonthermal radio filaments and X-ray features is also seen in high-resolution images of G0.11−0.08 (Yusef-Zadeh et al. 2002).

We extracted events from the isolated continuum X-ray feature G359.32−0.16. The events were selected from a $35.4'' \times 57.6''$ ellipse centered at $l = 359.43382^{\circ}$, $b = -0.09655^{\circ}$ with radius 4.15′ and 5.96′, respectively, with a position angle P.A. $= 38.6^{\circ}$. The background was estimated using a local background. After accounting for the background, the region contains only $45 \pm 16$ net photons (90% uncertainty) in the *Chandra* bandpass, all of which lie between 3.3 and 8.0 keV; in the 0.5–2.0 keV band there are <7 net counts, and in the 2.0–3.3 keV band there are <11 net counts. This does not provide enough signal to model the spectrum in detail. Therefore, following Muno et al. (2004b), we calculated a net photon flux of $1 \times 10^{-7}$ photons cm$^{-2}$ s$^{-1}$ and a hardness ratio $(h - s)/(h + s) = 0.2 \pm 0.4$, where $h$ is the number of counts in the 4.7–8.0 keV band and $s$ is the 3.3–4.7 keV band. If the absorption column to the source is $6 \times 10^{22}$ cm$^{-2}$, then we can use Figure 13 of Muno et al. (2004b) to estimate that the spectrum is consistent with a $\Gamma = 1$ power law with a luminosity of $1 \times 10^{33}$ ergs s$^{-1}$. Unlike other radio filaments in Sgr C, G359.32−0.16 does not seem to have a 6.4 keV correspondence; thus, it is possible that this X-ray feature is an X-ray synchrotron source similar to other X-ray/radio nonthermal filaments that have been detected in the Galactic center region (Sakano et al. 2003; Lu et al. 2003; Yusef-Zadeh et al. 2003).

In addition to radio filaments described above, Sgr C is surrounded by a number of additional weaker radio filaments that have been identified at 20 and 90 cm wavelengths (Nord et al. 2004; Yusef-Zadeh et al. 2004). We predict that large-scale sensitive X-ray observations of this region with *Chandra* and *XMM-Newton* should detect additional X-ray correspondence to radio features.

#### 3.1.3. $^{13}$CO *Line Emission*

The $^{13}$CO (1–0) emission in the vicinity of Sgr C spans a wide range of velocities, from approximately −200 to +200 km s$^{-1}$. Velocity channel maps in the −172 to 86 km s$^{-1}$ range, where the brightest emission occurs, are shown in celestial coordinates in Figure 4. A number of distinct velocity components can be identified, some with velocities forbidden by the Galactic rotation. The emission associated with the Sgr C molecular cloud is seen in the central part of the map in the −77 to −36 km s$^{-1}$ channels. In addition, an elongated feature approximately parallel to the Galactic plane is seen to the west of Sgr C at lower velocities (below −90 km s$^{-1}$). Another elongated feature, roughly perpendicular to the Galactic plane, is seen in the northeast part of the map at velocities above −25 km s$^{-1}$.

Molecular column densities can be computed using equation (8) of Lis & Goldsmith (1991) for a linear molecule:

$$N_{\rm tot} = \frac{4.0 \times 10^{12}\ {\rm cm}^{-2}}{J^2 \mu^2({\rm D}) B({\rm K})} Z \exp\left[\frac{E_J({\rm K})}{T_{\rm ex}}\right] \frac{1}{\eta} \int T_A^* \, dv \left({\rm K\ km\ s^{-1}}\right). \quad (3)$$

In our case, $J = 1$, the dipole moment $\mu = 0.112$ D, the rotational constant $B = 2.64$ K, the partition function $Z = T_{\rm ex}/B$, the upper level energy $E_1 = 2B$, and the main-beam efficiency $\eta = 0.4$. Therefore,

$$N_{\rm tot} = 1.14 \times 10^{14}\ {\rm cm}^{-2} T_{\rm ex} \exp\left(\frac{5.28}{T_{\rm ex}}\right) \int T_A^* \, dv \left({\rm K\ km\ s^{-1}}\right). \quad (4)$$

The assumption of optically thin emission is justified given the relatively low $^{13}$CO (1–0) line intensities compared to the peak line intensity observed in Sgr B2 (Lis & Goldsmith 1989). The dependence of the molecular column density on the excitation temperature is relatively mild, as the factor $T_{\rm ex} \exp(5.28/T_{\rm ex})$

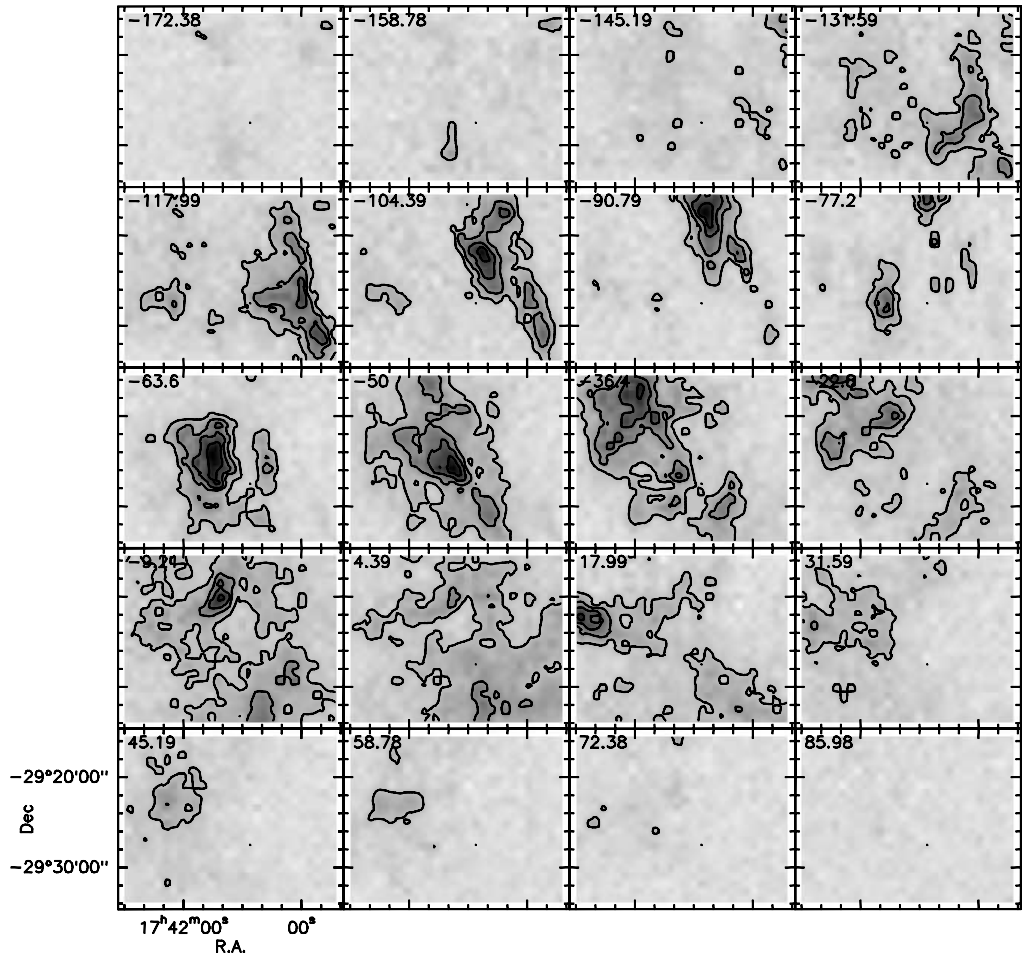


FIG. 4.—$^{13}$CO (1–0) velocity channel maps. Channel center velocities are given in the upper left corner of each panel. The emission associated with the Sgr C cloud is seen in the central part of the map in the −77 to −36 km s$^{-1}$ panels. Contour levels are −0.5, 0.5, 1, 1.5, and 2 K. The emission has been corrected for the atmospheric attenuation and warm losses, but not for the main-beam efficiency ($\eta = 0.4$). This figure is shown in J2000.0 celestial coordinates.

varies between 21 and 46 for $T_{\rm ex}$ between 15 and 40 K. In the subsequent analysis we assume $T_{\rm ex} = 25$ K (the cold component in the two-component gas model of Hüttemeister et al. 1993a) and the fractional $^{13}$CO abundance $X = 10^{-6}$, as determined for Sgr B2 (Lis & Goldsmith 1991), which gives

$$N_{\rm H_2} = 3.5 \times 10^{21}\ {\rm cm}^{-2} \int T_A^*\, dv\big({\rm K\ km\ s}^{-1}\big). \qquad (5)$$

The uncertainty in the molecular column densities is of order 40%, taking into account the uncertainties in the calibration and the excitation temperature.

The peak $^{13}$CO (1–0) intensity integrated over the −200 to 200 km s$^{-1}$ velocity range is 160 K km s$^{-1}$, and the average value over the area covered by our observations is 84 K km s$^{-1}$. The corresponding $H_2$ column densities are $5.6 \times 10^{23}$ and $2.9 \times 10^{23}$ cm$^{-2}$, respectively. Limiting the velocity range to −85 to −30 km s$^{-1}$, corresponding to the Sgr C cloud, results in the peak and average integrated line intensities of 80 and 22.3 K km s$^{-1}$, respectively. The corresponding $H_2$ column densities are $2.8 \times 10^{23}$ and $8 \times 10^{22}$ cm$^{-2}$, respectively. Assuming a distance of 8.5 kpc, the total $H_2$ mass contained within our map is $1.5 \times 10^6\ M_\odot$ in the −200 to 200 km s$^{-1}$ velocity range and $4 \times 10^5\ M_\odot$ in the −85 to −30 km s$^{-1}$ range. These values are much lower compared to the molecular mass of the Sgr B2 cloud $\sim 7 \times 10^6\ M_\odot$ (Lis & Goldsmith 1989), in agreement with the general weakness of the $^{13}$CO emission in Sgr C compared to Sgr B2.

#### 3.1.4. *The Morphology of* Fe K$\alpha$ *and* $^{13}$CO *Line Emission*

Figure 5*a* shows contours of $^{13}$CO line emission integrated over the velocity range between −77 and −22 km s$^{-1}$ superimposed on the gray-scale distribution of Fe K$\alpha$ 6.4 keV line emission from Sgr C. The strongest molecular line emission has a velocity of −65 km s$^{-1}$, which identifies the Sgr C molecular cloud (Liszt & Spiker 1995). An isolated molecular feature near $b \sim -3'$ arises from the −120 to −90 km s$^{-1}$ molecular cloud. The strongest 6.4 keV line emission of G359.48−0.15 arises from the western portion of the molecular cloud. The second strongest 6.4 keV peak emission is about 2′ southwest of G359.48−0.15. These faint X-ray features are correlated better with the fainter lower velocity components near −40 km s$^{-1}$. It is clear that the overall distribution of the 6.4 keV emission follows the western edge of the −65 km s$^{-1}$ molecular cloud, as there is no X-ray emission from the eastern edge of the molecular cloud. Figure 5*b* shows another version of Figure 5*a* except that contours of $^{13}$CO emission are superimposed on the gray-scale X-ray continuum emission. The continuum X-ray emission from the Sgr C complex is also consistent with being distributed to the western edge

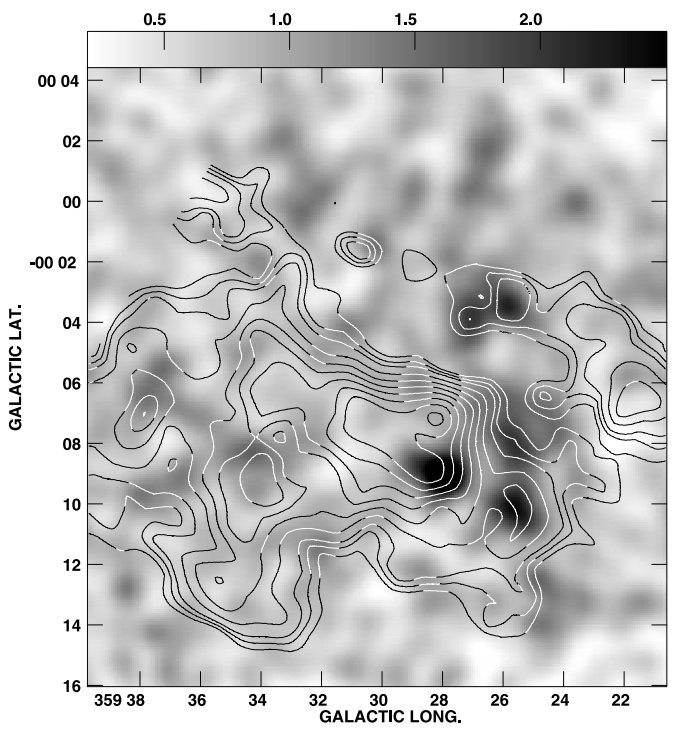


FIG. 5*a*

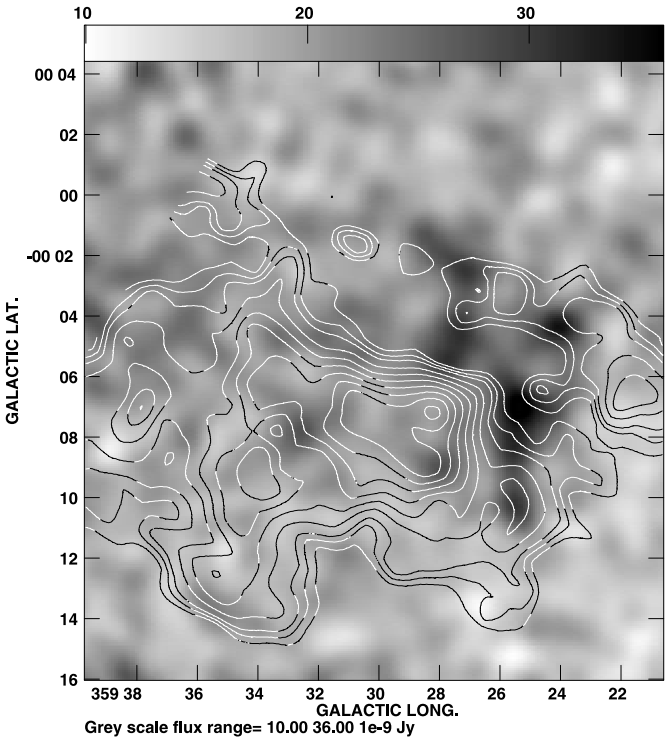


FIG. 5*b*

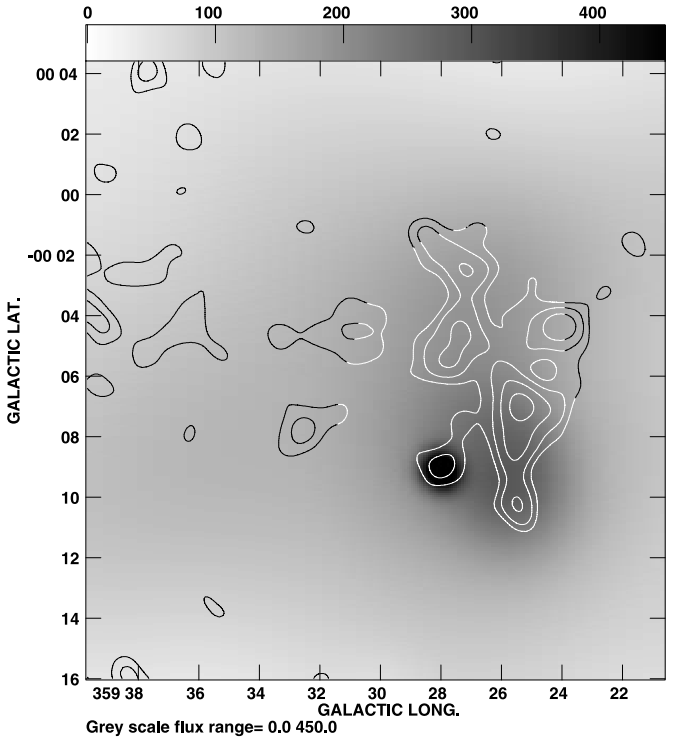


FIG. 5*c*

FIG. 5.—(*a*) Contours of velocity-integrated $^{13}$CO emission between $-77.2$ and $-22$ km s$^{-1}$ superimposed on a gray-scale 6.4 keV K$\alpha$ line emission with a 30″ resolution. Contour levels are set at (2, 2.25, 3, 3.5, 4, 4.5, 5, 5.5, 6) $\times$ 14 K km s$^{-1}$. (*b*) Similar to (*a*), except that the gray scale shows the continuum X-ray emission with 60″ spatial resolution between 2 and 6 keV. (*c*) Contours of X-ray continuum emission superimposed on a gray-scale equivalent width map of 6.4 keV line emission.

of the $-65$ km s$^{-1}$ molecular cloud. This suggests that the fluorescent 6.4 keV line emission and the X-ray continuum emission trace each other, although the line-to-continuum ratio may vary across the cloud. Moreover, the nonthermal filaments (see Figs. 1 and 3) are detected only at the western edge of the Sgr C cloud. These images suggest the correspondence of K$\alpha$ line and nonthermal radio emission at the western edge of the Sgr C molecular cloud.

We also note that distribution of the equivalent width of the Fe K$\alpha$ line is strongest to the west of the $-65$ km s$^{-1}$ molecular

TABLE 2
PARAMETERS OF X-RAY FIT TO GALACTIC CENTER CLOUDS

| Region | Area (arcmin$^2$) | Fe K$\alpha$ Flux (photons cm$^{-2}$ s$^{-1}$) | Fe K$\alpha$ EW (eV) | Flux (2–8 keV) (ergs cm$^{-2}$ s$^{-1}$) | Dereddened Flux (ergs cm$^{-2}$ s$^{-1}$) |
|---|---|---|---|---|---|
| Sgr C | 77 | $7.2\ (0.2) \times 10^{-5}$ | 470 (100) | $9.1\ (0.1) \times 10^{-12}$ | $1.2\ (0.2) \times 10^{-11}$ |
| Radio arc | 123 | $3.5\ (0.1) \times 10^{-4}$ | 670 (50) | $3.7\ (0.1) \times 10^{-11}$ | $5.6\ (0.1) \times 10^{-11}$ |
| Arches cluster | 1.6 | $1.3\ (0.1) \times 10^{-5}$ | 810 (200) | $9.1\ (0.1) \times 10^{-13}$ | $1.2\ (0.2) \times 10^{-12}$ |
| Sgr B1 | 77 | $8.6\ (4) \times 10^{-5}$ | 570 (70) | $7.6\ (0.1) \times 10^{-12}$ | $9.7\ (0.7) \times 10^{-12}$ |
| Sgr B2 | 96 | $2.4\ (0.1) \times 10^{-4}$ | 1150 (150) | $9.5\ (0.1) \times 10^{-12}$ | $1.1\ (0.1) \times 10^{-11}$ |

cloud with a value of 450 eV. This peak coincides with the peak of $^{13}$CO emission at $-65$ km s$^{-1}$ at G359.47$-$0.15. Figure 5*c* shows contours of 2–6 keV X-ray emission superimposed on the 6.4 keV equivalent width image of Sgr C. The intensity of the Fe K$\alpha$ line emission toward Sgr C is quite high, $\sim 6^{+2}_{-4} \times 10^{-6}$ photons cm$^{-2}$ s$^{-1}$ arcmin$^{-2}$, which is within at least a factor of $\sim$2 larger than the average value in the central 20 pc of the Galactic center. Table 2 lists the parameters of the fit to the Sgr C region. The equivalent width of the Fe K$\alpha$ line is not sensitive to the uncertainty introduced by the absorption.

The distribution of 6.4 keV line emission based on *ASCA* observations was compared with that of CS (1–0) line emission from Sgr C (Murakami et al. 2001b). However, the high negative velocity molecular gas with the velocity interval between $-120$ and $-110$ km s$^{-1}$ was compared with their low spatial resolution X-ray data. They assumed that the core of Sgr C is centered on the high negative velocity feature at $-110$ km s$^{-1}$. However, the core of Sgr C and the bulk of molecular gas are known to have a velocity of $-65$ km s$^{-1}$ (see Figs. 5*a* and 5*b*), as a number of ionized and molecular studies have indicated (e.g., Tsuboi et al. 1991; Liszt & Spiker 1995; Lis & Carlstrom 1994). In order to make a more detailed comparison of our X-ray and radio continuum data with the $-110$ km s$^{-1}$ molecular feature, we used the same CS (1–0) molecular line data (Tsuboi et al. 1999) that Murakami et al. (2001b) had used. The distribution of $^{13}$CO is quite similar to CS (1–0), suggesting that both trace the overall molecular gas distribution in the region. Figures 6*a* and 6*b* show contours of CS (1–0) emission in the $-120$ to $-110$ km s$^{-1}$ velocity interval superimposed on the 6.4 keV line and 90 cm continuum distributions, respectively. We agree with the Murakami et al. (2001b) assessment that K$\alpha$ line emission at the position of $l = 359^\circ 26'$ lies at the edge of one of the CS peaks at this velocity interval. However, there is no evidence of a strong K$\alpha$ emission counterpart to the CS peaks at positive Galactic latitudes. Figure 6*b* shows that the nonthermal Sgr C filament lies also at the edge of the $-110$ km s$^{-1}$ velocity feature. The morphology of a

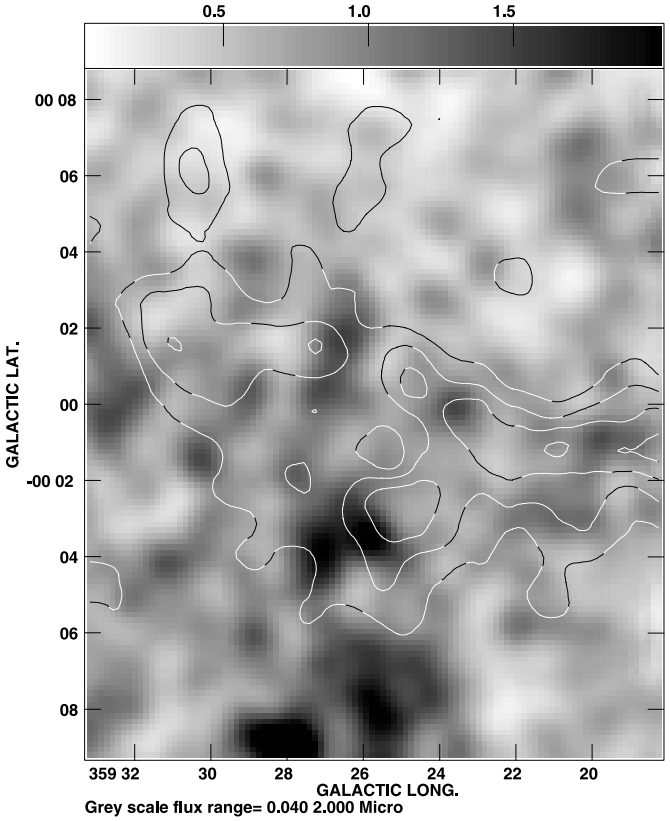


FIG. 6*a*

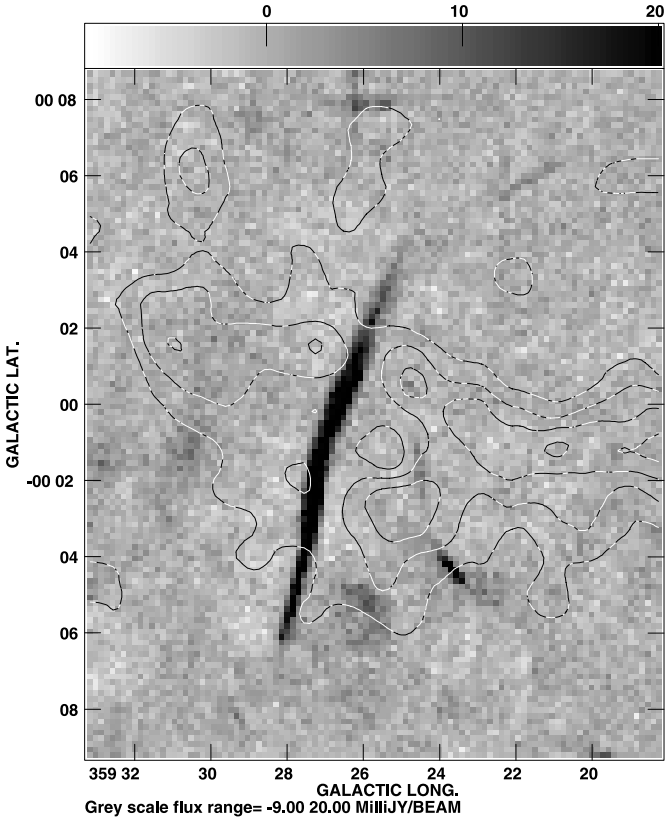


FIG. 6*b*

FIG. 6.—(*a*) Plot of the spectral index distribution along the brightest nonthermal vertical filament of Sgr C. (*b*) Similar to (*a*), except that the slice plot shows 1 $\sigma$ error bars of the spectral index distribution. These measurements are based on the 20 and 90 cm images convolved to a Gaussian beam having FWHM = 12.6 arcsec$^2$.

nonthermal filament lying at the edge of K$\alpha$ line emitting molecular gas is also made for the $-110$ km s$^{-1}$ velocity feature of Sgr C. Thus, the LECRs from the Sgr C filament could also be responsible for the origin of K$\alpha$ 6.4 keV line emission from the high negative velocity component, as discussed in more detail below. Thus, there are two issues that weaken the application of the irradiation model to the $-110$ km s$^{-1}$ cloud. One is that the $^{13}$CO integrated intensity in the $-200$ to 200 km s$^{-1}$ velocity interval averaged over the area mapped is 84 K km s$^{-1}$. The corresponding value for the $-120$ to $-110$ km s$^{-1}$ velocity range is 9.5 K km s$^{-1}$. One of the questions that arises is that the X-ray radiation nebula model would thus have to explain why only 11% of the molecular gas on the line of sight is irradiated assuming that the $-110$ and $-65$ km s$^{-1}$ velocity components are part of the Sgr C cloud. The other is the lack of 6.4 keV emission from other peaks of the $-110$ km s$^{-1}$ cloud facing toward Sgr A$^*$.

There is no X-ray counterpart to the edge of the cloud in our *Chandra* and *XMM-Newton* data when compared with Figure 1 of Murakami et al. (2001b). A number of reasons could be potentially responsible for this discrepancy. One is the low-resolution map based on their *ASCA* measurements that could be contaminated by point sources within 6.1–7 keV; there are not enough point sources to account for the excess emission. The other is their line width being different, 6.1–7.1 keV versus 5.8–7.0 keV. Lastly, time variability of the iron flux is also a possibility over the course of 8 yr. However, the comparison of the iron flux from a knotlike feature at G359.48$-$0.15 with that of Murakami et al. (2001b) requires about 24 lt-yr to explain the shift in the centroid of this knotlike feature. In addition, the derived EW (460 $\pm$ 100 eV) seems to be lower than the value (800 eV) obtained by Murakami et al. (2001b). We believe that the main reason for the difference is that we used different assumptions for the background emission. Murakami et al. (2001b) used an off-source region for the background, so their subtraction is both of particle background and (an estimate of) the Galactic diffuse emission. Our images were subtracted only by the particle background. Lastly, the excess emission could be due to a transient behind a cloud.

If the fractional $^{13}$CO abundance in Sgr C is lower than in Sgr B2, the column density estimate could be higher. However, the $^{12}$C/$^{13}$C ratio is $\sim$20 in the Galactic center compared to the local value of 77 $\pm$ 7 (Wilson & Rood 1994). With $X(\mathrm{CO}) = 10^{-4}$, the "nominal" Galactic center $^{13}$CO abundance is $X(^{13}\mathrm{CO}) = 4 \times 10^{-6}$. The low value of $X(^{13}\mathrm{CO}) = 10^{-6}$ that we used is already low and is more consistent with the local ISM value (e.g., Frerking et al. 1982). This suggests that the estimated $^{13}$CO abundance cannot be lower.

Another useful method that traces the column density of molecular hydrogen is submillimeter emission. Figure 7 shows a gray-scale 850 $\mu$m image of Sgr C based on SCUBA observations (Pierce-Price et al. 2000) and contours of $^{13}$CO line emission. Two submillimeter peaks are noted: the northeastern component is the site of a star-forming region associated with the $-65$ km s$^{-1}$ Sgr C cloud, whereas the southeastern component is unlikely to be related to the Sgr C cloud. The peak submillimeter emission that lies in the vicinity of the peak of the molecular line emission has a flux density of 7.44 Jy per 15 arcsec$^2$. The peak column density is then estimated to be $\sim 6 \times 10^{23}$ cm$^{-2}$ using the value of 513 $M_\odot$ Jy$^{-1}$ at 850 $\mu$m, as derived by Pierce-Price et al. (2000). The mean value of the column density of the Sgr C cloud from submillimeter observations is about $2 \times 10^{23}$ cm$^{-2}$. This value is consistent with earlier estimates of the column density determined by Lis & Carlstrom (1994).

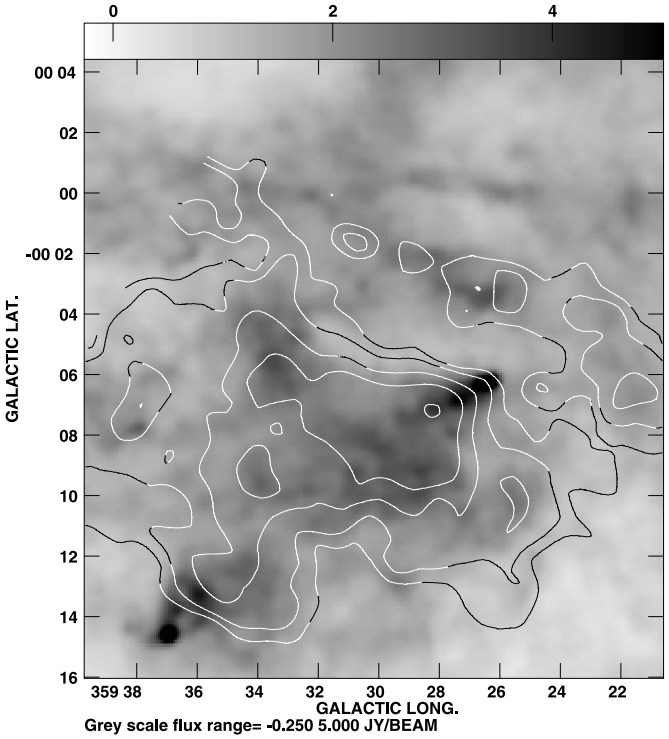


FIG. 7.—Contours of $^{13}$CO molecular line emission superimposed on a gray-scale submillimeter image at 850 $\mu$m taken from Pierce-Price et al. (2000) convolved to a resolution of 15″.

### 3.1.5. *Spectral Index Measurements*

We obtained a spectral index $\alpha$ (where flux density $F_\nu \propto \nu^\alpha$) distribution of Sgr C by using the 90 and 20 cm images (Nord et al. 2004; Yusef-Zadeh et al. 2004), convolved with an FWHM Gaussian 12.6″ $\times$ 12.6″. Radio continuum emission from Sgr C at 90 cm is an excellent probe of nonthermal sources in this complex source. Figure 8*a* shows a slice cut of the spectral index distribution along the brightest filament, whereas Figure 8*b* shows the error plot of the spectral index distribution. The spectral index is typically ranging between $-1 \pm 0.3$ and $-0.7 \pm 0.1$ to the south and to the north of the linear filament away from the Galactic plane, respectively. The emission from the Sgr C H II region at 20 cm is mainly responsible for the large error in the value of $\alpha$ to the south of the filament. These measurements are consistent with the spectral index values between $-0.7$ and $-1$, as determined between 20 and 6 cm (Liszt & Spiker 1995). We also compared the 3.6 and 2 cm images of the bright nonthermal filament and found a steepening of the spectral index at shorter wavelengths.

Figures 9*a* and 9*b* show the 3.6 and 2 cm images, respectively, with a resolution of 6.8″ $\times$ 6.4″ (P.A. = 10.2°). We note that the vertical filament is detected prominently at 3.6 cm with a typical surface brightness of $\sim$3 mJy beam$^{-1}$. However, the upper limit to the brightness of the filament is about 0.4 mJy beam$^{-1}$ at 2 cm. This filament was not detected at 1.2 cm either (Tsuboi et al. 1991). Accurate spectral index measurements restricting the *uv* range to 2 and 30 k$\lambda$ for both the 3.6 and 2 cm data show that the spectral index of the bright filament is equal to or steeper than $-2.3 \pm 0.5$. This suggests a break in the spectral index of nonthermal filaments from 90 to 2 cm, possibly due to the shorter lifetime of more relativistic particles at high energies. Previous spectral index measurements of other Galactic center filaments show similar spectral index break with a value of roughly $-2$ at shorter wavelengths than at 6 cm (Lang et al. 1999). The first

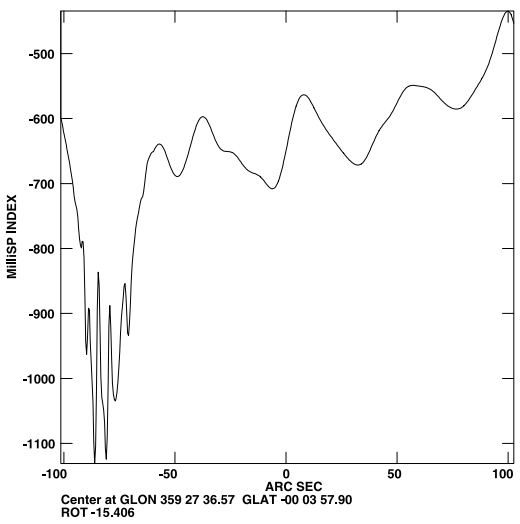


FIG. 8*a*

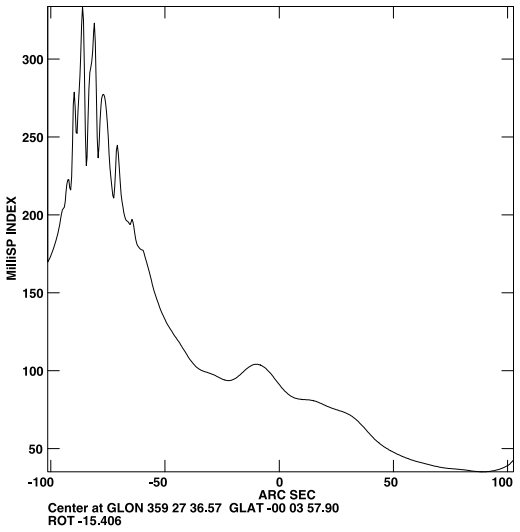


FIG. 8*b*

FIG. 8.—(*a*) Plot of the spectral index distribution along the brightest nonthermal vertical filament of Sgr C. (*b*) Similar to (*a*), except that the slice plot shows 1 $\sigma$ error bars of the spectral index distribution. These measurements are based on the 20 and 90 cm images convolved to a Gaussian beam having FWHM = 12.6 arcsec[2].

detection of polarized emission from Sgr C, as shown in Figure 10, is described in the Appendix.

### 3.2. *Galactic Center Molecular Clouds at $l > 0^\circ$*

#### 3.2.1. 6.4 keV *Emission*

With the exception of the Sgr C molecular cloud that lies beyond Sgr A and at the negative longitude side of the Galactic center, the largest concentration of dense and warm molecular clouds is known to be distributed near Sgr A and in the positive longitude side of the Galactic center region (e.g., Morris & Serabyn 1996; Tsuboi et al. 1999). Four of the well-known molecular cloud complexes are the "20 km s$^{-1}$ cloud" (M$-$0.13$-$0.05) distributed near Sgr A, the "45 km s$^{-1}$ cloud," the "$-$30 km s$^{-1}$ cloud," both of which extend between Sgr A and the radio arc at $l \sim 0.2^\circ$, and the molecular ridge extending from molecular cloud M0.25$-$0.01 to Sgr B2. The 45 and $-$30 km s$^{-1}$ clouds lie on one side of the radio arc and overlap with each other spatially. The largest concentration of bright and long nonthermal radio filaments is also found on the positive longitude side of the Galactic center (Yusef-Zadeh

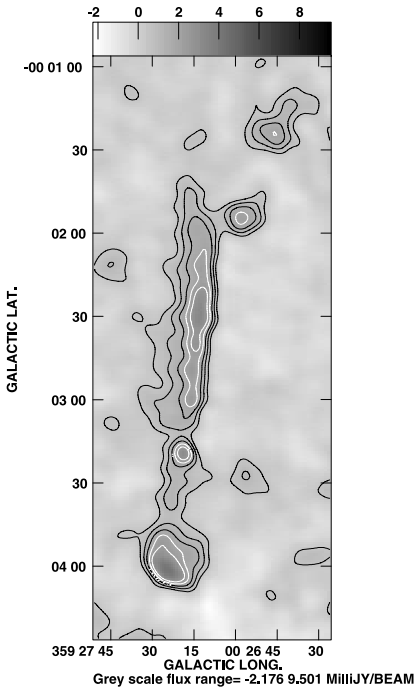


FIG. 9*a*

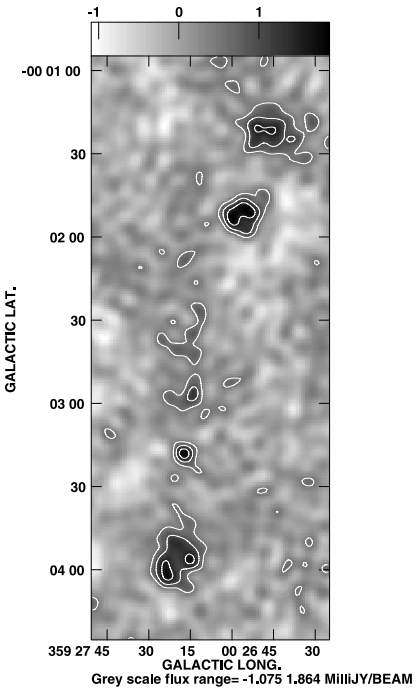


FIG. 9*b*

FIG. 9.—(*a*) Gray-scale continuum image of the bright filament of Sgr C at 3.6 cm with contours set at 0.25 $\times$ (2, 4, 6, 8, 10) Jy beam$^{-1}$. The rms noise is 0.24 mJy and the spatial resolution is 6.8″ $\times$ 6.4″ (P.A. = 10.2°). (*b*) Identical to (*a*), except that 2 cm contours are set at 0.25 $\times$ (2, 4, 6) Jy beam$^{-1}$. Both images are constructed by using the same *uv* range (2–30 k$\lambda$) to ensure the same spatial frequency coverage.

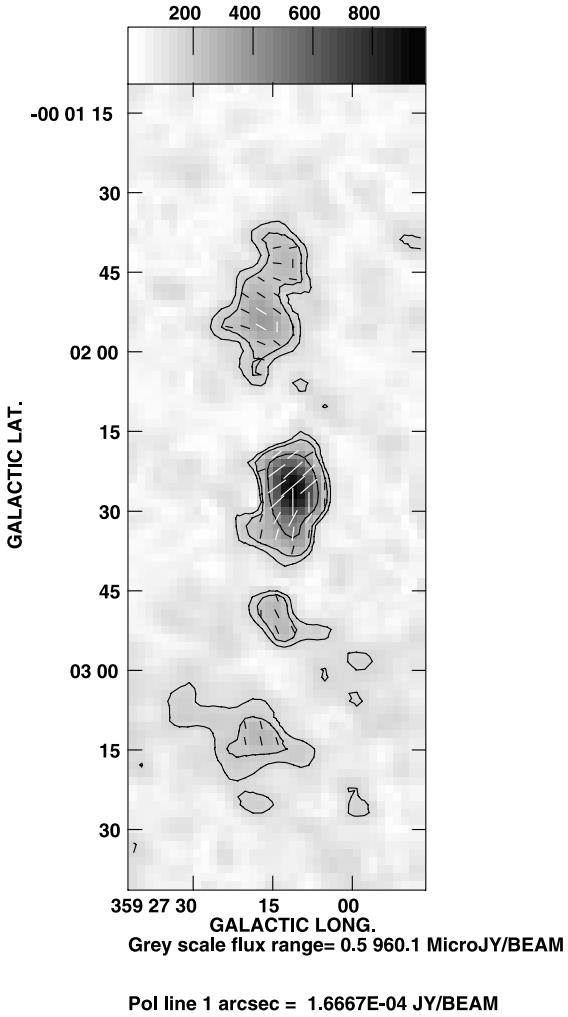


Fig. 10*a*

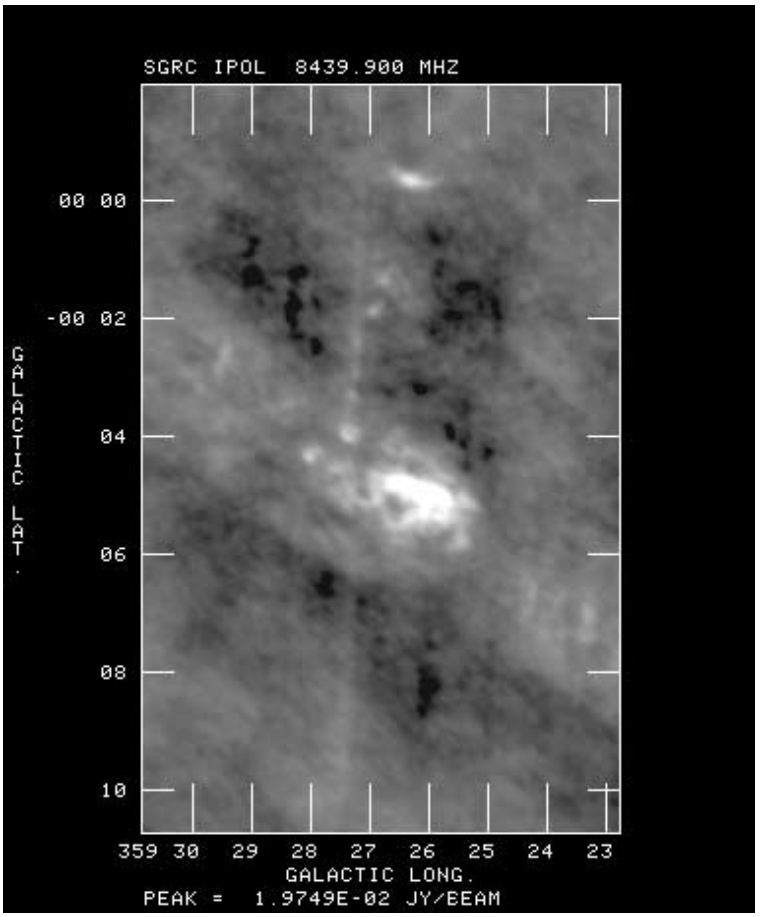


Fig. 10*b*

Fig. 10.—(*a*) Gray-scale linearly polarized continuum emission from the bright filament of Sgr C at 3.6 cm with contours set at 0.15, 0.2, and 0.4 mJy beam$^{-1}$ and the resolution of $7.9'' \times 6.7''$ (P.A. $= -6.6^{\circ}$). The length of the line segments presents the strength of the polarized emission ($1''$ corresponds to 0.166 mJy beam$^{-1}$), whereas the position angle of the line segments shows the polarization angle distribution. (*b*) Gray-scale image of Sgr C at 3.6 cm with a resolution of $9.8'' \times 7.5''$ (P.A. $= -7.5^{\circ}$). This image is not corrected for the response of the primary beam. The weak filament to the south lies outside the FWHM of the primary beam.

et al. 1984). The radio arc and its adjacent molecular clouds can potentially provide evidence for a mixture of interacting thermal and nonthermal features. Given that relativistic particles of the Sgr C filaments are interacting with its molecular cloud, we believe that the interaction of nonthermal particles of the radio arc with its adjacent molecular clouds can also explain the nature of 6.4 keV emission, as described below.

To illustrate the proposed physical association between nonthermal radio filaments, the 45 and $-30$ km s$^{-1}$ molecular clouds, and the 6.4 keV line emission, Figures 11*a* and 11*b* show gray-scale views of the nonthermal radio filaments of the radio arc and Sgr A at 20 cm against the fluorescent 6.4 keV image and ammonia distribution (Güsten et al. 1981; Yusef-Zadeh 1986). Figure 11*a* shows the distribution of the K$\alpha$ EW line emission in green and a 20 cm continuum image in red, whereas the $NH_3(1, 1)$ line emission from the "20 and 45 km s$^{-1}$ clouds" is displayed in Figure 11*b* as contours with a spatial resolution of $40''$. Given that ammonia line observations have lower resolution than radio continuum and X-ray observations, the overall distribution of bright knots of K$\alpha$ EW line emission correlates well with peaks of ammonia line emission associated with the 45 km s$^{-1}$ molecular cloud. We note that there is no evidence for strong compact or diffuse K$\alpha$ line emission from the 20 km s$^{-1}$ cloud. This cloud is one of the most prominent dust continuum features in the Galactic center showing high mass and column density. Furthermore, nonthermal filaments have been detected toward this cloud. Similarly, another massive cloud that shows a lack of EW of K$\alpha$ line emission is M+0.25+0.01. Individual compact ammonia clumps of the 45 km s$^{-1}$ molecular cloud that have 6.4 keV line correspondence, as shown in Figure 11*b*, are M0.06$-$004, M0.10$-$0.01, M0.11$-$0.08, M$-$0.02$-$0.07, and M0.07$-$0.08 (e.g., Serabyn & Güsten 1987; Lang et al. 2002). The molecular clump M0.11$-$0.08 lies closest in projection to the nonthermal filaments of the arc and has been extensively mapped recently in CS, SiO, and $H^{13}CO^+$ lines. This clump has velocities ranging between 15 and 45 km s$^{-1}$ and has a strong 6.4 keV line counterpart (Tsuboi et al. 1997; Yusef-Zadeh et al. 2002; Handa et al. 2006).

Another cloud that is dynamically coupled to the thermal component of the radio arc is the $-30$ km s$^{-1}$ cloud (Serabyn & Güsten 1987). This cloud is distributed on the positive latitude side of

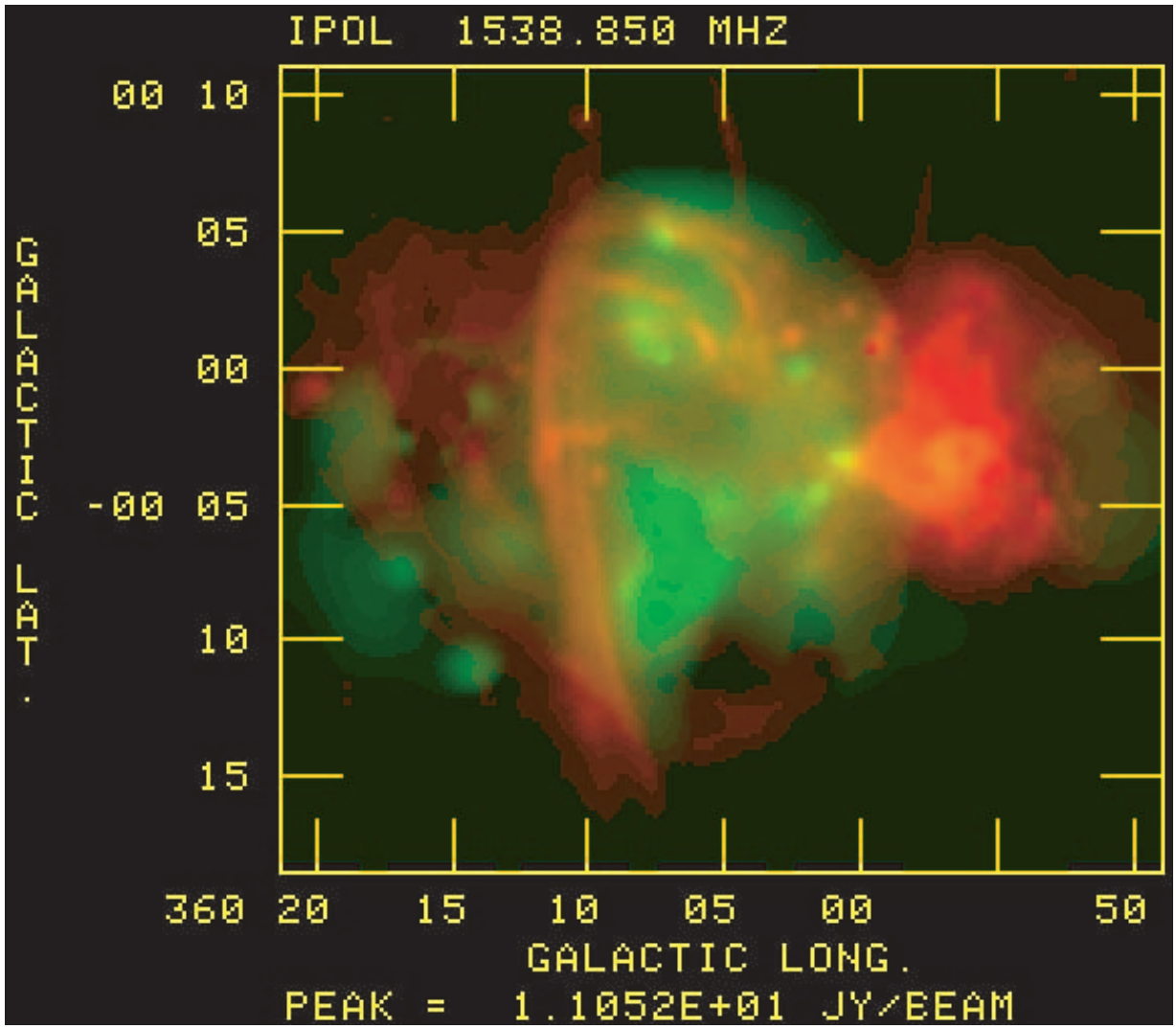


FIG. 11*a*

FIG. 11.—(*a*) A 20 cm continuum image of the Sgr A complex and the radio arc in Galactic coordinates (*red*) shown against the distribution of the 6.4 keV K$\alpha$ line emission (*green*). (*b*) A 20 cm continuum image of the Sgr A complex and the radio arc in Galactic and celestial coordinates against contours of ammonia line emission from prominent molecular clouds in the Galactic center region (Güsten et al. 1981; Yusef-Zadeh 1986). (*c*) Gray-scale image of the 6.4 keV line EW distribution with contours set at (1, 1.5, 2, 2.5, 3, 3.5, 4, 5, 6, 8, 10, 14, 18) $\times 10^2$ eV. The plus signs show the ammonia peaks, as shown in (*b*), and the five-pointed stars show the peak position of C line emission from Serabyn & Güsten (1987).

the arc and is associated with thermal gas of the arched filaments that is ionized by the Arches cluster G0.121+0.017 (e.g., Cotera et al. 1996; Figer et al. 1999; Lang et al. 2002). The comparison of the distributions of the CS molecular gas and K$\alpha$ line emission suggests that the K$\alpha$ line peaks follow the distribution of the CS emission (Serabyn & Güsten 1987). In fact, one of the ammonia peaks M$-$0.02$-$0.05 ($-15$ km s$^{-1}$), as shown in Figure 11*b*, coincides with a southern extent of the $-30$ km s$^{-1}$ molecular cloud. M$-$0.02$-$0.05 and the CS peaks 1 and 2 identified by Serabyn & Güsten (1987) have 6.4 keV line correspondence. Lastly, another knotlike K$\alpha$ line emission G0.12+0.00 distributed in the immediate vicinity of Arches cluster G0.121+0.017 appears to be associated with a CS molecular emission (Lang et al. 2002; Serabyn & Güsten 1987).

The hook-shaped structure noted in the K$\alpha$ EW line distribution correlates extremely well with the ammonia distribution, as noted in Figures 11*a* and 11*b*. In addition, nonthermal emission from magnetized filaments and the recent detection of nonthermal emission from the Arches cluster provide another source for the interaction of cosmic rays with molecular gas to explain the origin of the 6.4 keV line emission. Although the total mass of molecular gas and radio continuum flux of nonthermal emission in the arc region are much higher than those in Sgr C, the column density of molecular gas and the EW of the K$\alpha$ line of about a few hundred eV are similar to those of Sgr C. With the exception of the G0.11$-$0.08 molecular cloud, which is closest to the filaments in projection having a hydrogen column density of (7–8) $\times 10^{23}$ cm$^{-2}$, the peaks of the 45 and $-30$ km s$^{-1}$ clouds show column densities of a few times $10^{23}$ cm$^{-2}$ (Güsten et al. 1981; Serabyn & Güsten 1987). The density and temperature of molecular gas from these clouds are also estimated to be about a few times $10^4$ cm$^{-3}$ and 50–80 K, respectively.

In the context of the LECR model, these characteristics imply that cosmic-ray particles penetrating molecular clouds should be uniform with similar metallicity as discussed in more detail in § 4.2. We measured the K$\alpha$ line and continuum X-ray flux of the

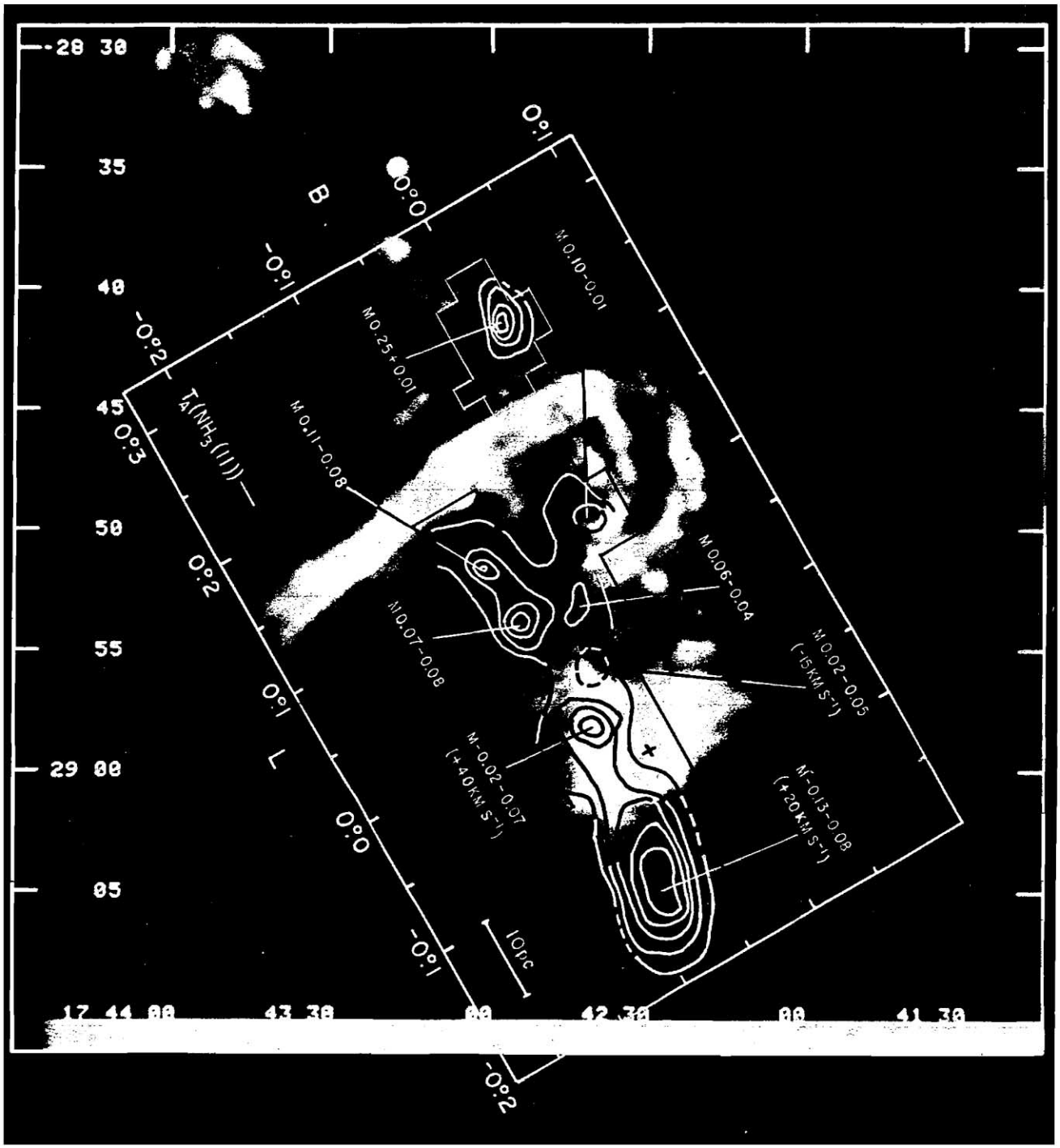


FIG. 11*b*

arc by taking a spectrum over an area of 123 arcmin$^2$ encompassing both 45 and $-30$ km s$^{-1}$ molecular clouds. An absorbed power law plus Gaussians were used to model all of the line emission. This model is not physically motivated but allows us to measure fluxes and equivalent widths. The dereddened continuum flux between 2 and 8 keV, Fe K$\alpha$ EW, and Fe K$\alpha$ flux are $5.6 \times 10^{-11}$ ergs cm$^{-2}$ s$^{-1}$, 670 eV, and $3.5 \times 10^{-4}$ photons cm$^{-2}$ s$^{-1}$, respectively. The parameters of the fits to Sgr C, the radio arc, Sgr B1, and Sgr B2 are shown in Table 2. These parameters are derived assuming a model of a power-law continuum under which the absorption columns are estimated to be lower than in thermal plasma models by a factor of 2–3. This results in a 30% lower estimated flux for the line from Sgr C, which should be taken as the systematic uncertainty in the measurement.

To examine the impact of LECR particles with molecular gas throughout the Galactic center, we also list in Table 2 the fitted parameters to two other Galactic center molecular cloud complexes Sgr B1 and B2. These clouds are associated with the

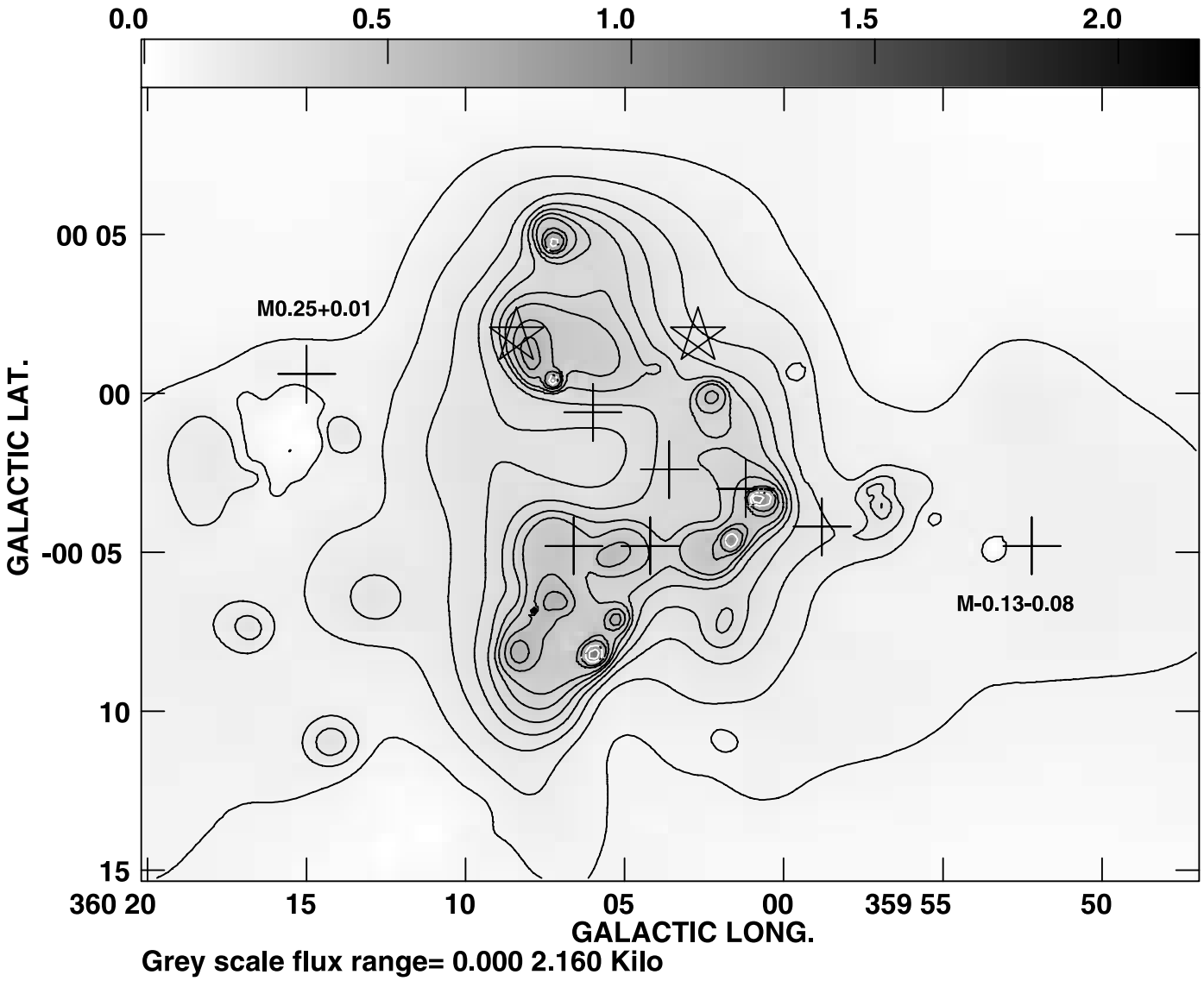


FIG. 11*c*

molecular ridge that extends between G0.25+0.01 and Sgr B2, as shown in Figure 2. Both of these clouds have been extensively studied in millimeter and submillimeter wavelengths, as well as in the K$\alpha$ line (e.g., Hüttemeister et al. 1993b; Lis & Carlstrom 1994; Murakami et al. 2001a, 2001b). The regions from which spectra were extracted from Sgr C, the radio arc, Sgr B1, and Sgr B2 are drawn on a large-scale 6.4 keV EW line distribution, as displayed in Figure 2. A more detailed study of the individual 6.4 keV line features will be given elsewhere.

#### 3.2.2. TeV *Emission*

Recent observation with HESS has discovered large-scale diffuse TeV emission from the inner 200 pc of the Galaxy (Aharonian et al. 2006). The morphology of diffuse emission correlates well with the distribution of CS molecular clouds, thus suggesting that the $\gamma$-ray emission is a product of the interaction of cosmic rays with interstellar gas near the Galactic center. These authors show that the spectrum of TeV emission from resolved clouds toward the Galactic center has a photon index $\Gamma \sim 2.3$, which is harder than that in the Galactic disk. They note that the $\gamma$-ray flux above 1 TeV is a factor of 3–9 times higher than in the Galactic disk and argue for an additional population of cosmic rays in this unique region. They propose that the TeV emission is due to hadronic interaction of cosmic rays with the target material. Their argument against the importance of TeV electrons is the short lifetime of their energies.

Given that the target material is the same, we compared the distribution of TeV emission with that of the 6.4 keV emission from molecular gas toward the Galactic center. Figure 12*a* shows contours of diffuse TeV emission superimposed on a gray-scale image of K$\alpha$ 6.4 keV line emission. The prominent TeV peaks are seen toward Sgr C, the radio arc, and Sgr B. Due to the subtraction of the compact and bright source coincident with Sgr A$^*$, it is not clear if the weak feature near G359.83$-$0.1 is real or due to an artifact of subtraction (J. Hinton 2006, private communication). As expected, there is a strong concentration of 6.4 keV knots that correlates well with the peaks of TeV emission toward Sgr C, Sgr B, and the arc. The brightest TeV emission from diffuse Galactic center molecular clouds is detected toward the radio arc followed by Sgr B2 and Sgr C. We also note that both the TeV and K$\alpha$ line emissions from the well-known "20 km s$^{-1}$" molecular cloud G$-$0.13$-$0.08 are weak. To illustrate the relationship between molecular gas, nonthermal filaments, and the fluorescent line emission, Figure 12*b* shows the contour distribution of submillimeter

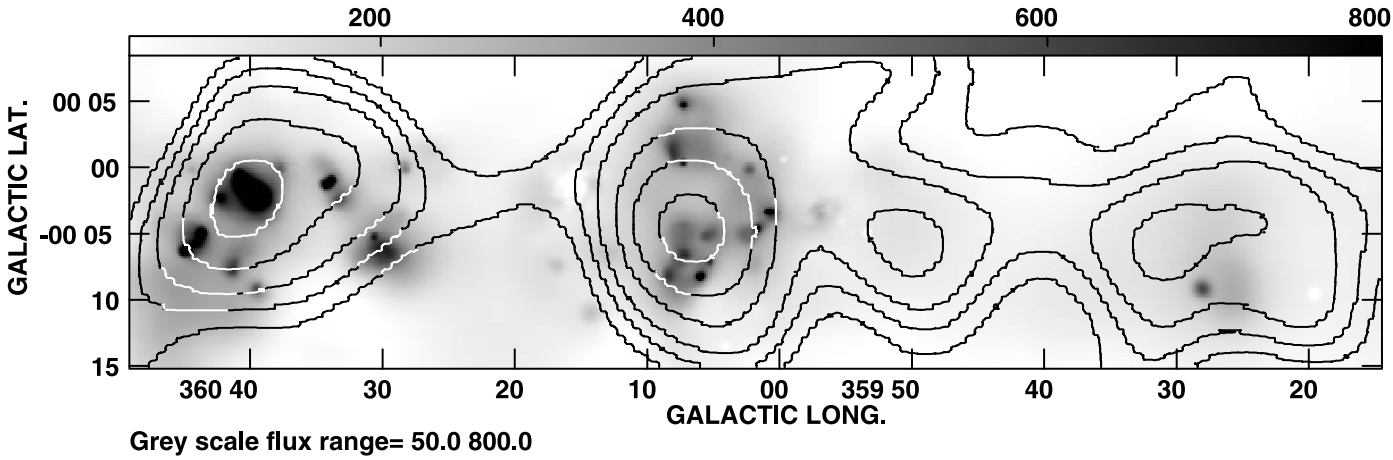


FIG. 12*a*

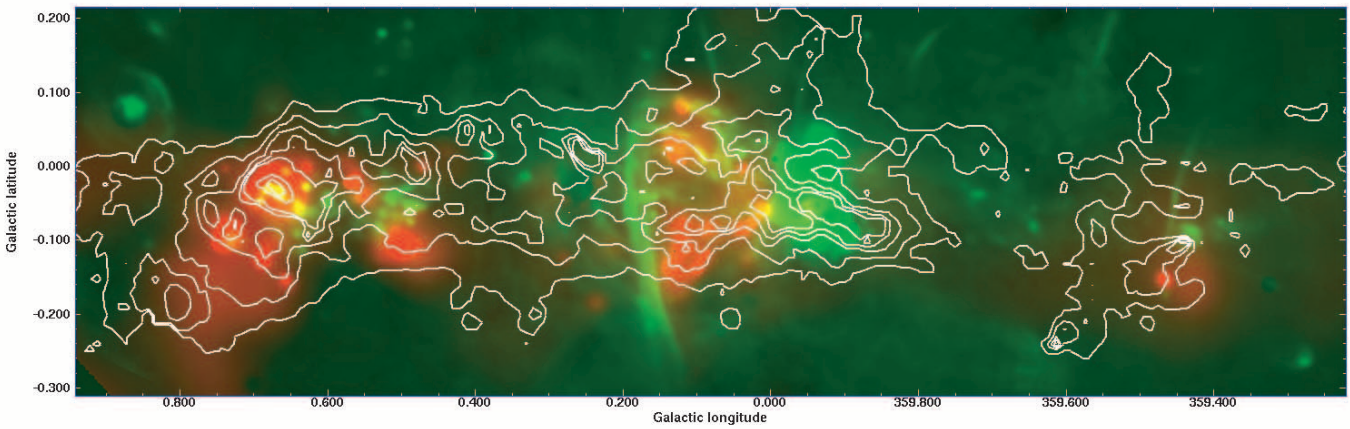


FIG. 12*b*

FIG. 12.—(*a*) Contours of HESS emission from the Galactic center (Aharonian et al. 2006) superimposed on the distribution of K$\alpha$ 6.4 keV EW line emission. (*b*) Contours of 850 $\mu$m submillimeter emission superimposed on the distributions of K$\alpha$ 6.4 keV EW line emission (*red*) and a 20 cm continuum emission (*green*).

emission distributed against a 20 cm continuum emission (*green*) and 6.4 keV emission (*red*). All of the prominent molecular clouds are represented in the submillimeter image.

## 4. DISCUSSION

There are three different types of observations that are used in support of large-scale high-energy activity in the inner few hundred parsecs of the Galactic center. These observations suggest that this activity is more pronounced than that observed in the disk of the Galaxy for the following reasons. One is the distribution of nonthermal radio emission traced by magnetized radio filaments, a 1° scale diffuse structure, known as the Galactic center lobe, a high concentration of confirmed supernova remnants such as G0.0+0.0 or Sgr A East (Ekers et al. 1983), G0.3+0.0 (Kassim & Frail 1996), G0.9+0.1 (Helfand & Becker 1987), G1.0−0.1 or Sgr D (Downes et al. 1979), and G359.1−0.5 (Downes et al. 1979), as well as nonthermal emission from colliding winds of massive stars in dense stellar clusters. These sources altogether signify regions of enhanced synchrotron emissivity (e.g., Gray 1994; Nord et al. 2004; Yusef-Zadeh et al. 2004; Law 2007). The recent detection of diffuse low-frequency radio continuum emission (LaRosa et al. 2006), as well as other indirect measurements (Yusef-Zadeh 2003), suggests that the large-scale diffuse distribution of the magnetic field cannot be too different than that observed in the Galactic disk. This is consistent with the picture that the Galactic center nonthermal radio filaments are expected to have a stronger magnetic field than that of the surrounding diffuse and weakly magnetized medium. Recent interpretation of the nonthermal filaments suggests that kinematic dynamo enhances the magnetic field in a medium that is initially threaded by weak magnetic field (Boldyrev & Yusef-Zadeh 2006). Thus, we suggest that cosmic-ray electron density of the diffuse gas must be enhanced in the Galactic center region in order to account for the excess synchrotron emissivity detected toward the central 200 pc of the Galaxy. Other recent measurements come from $H_3^+$ and $H_3O^+$ observations, suggesting that the ionization rate due to cosmic rays has to be higher by 1–2 orders of magnitude in the Galactic center region than in the disk (Oka et al. 2005; van der Tak et al. 2006). Lastly, the recent discovery of diffuse TeV emission from the Galactic center molecular clouds shows enhanced $\gamma$-ray emission at higher energies having a spectrum that differs from that of the cosmic rays in the disk of the Galaxy.

Based on the above arguments, it is natural to consider the possibility that enhanced cosmic rays in the Galactic center region

could play an important role in accounting for much of the observed high-energy activity in this region. This hypothesis stems from the fact that a great deal of warm and dense molecular gas is distributed in the central region (e.g., Rodriguez-Fernandez et al. 2001); thus, the widely distributed molecular gas can be used as an excellent target by the impact of enhanced cosmic rays. In particular, the origin of the observed 6.4 keV emission throughout the Galactic center region can be tied to the impact of LECR electrons with molecular gas. The role of LECRs was first proposed to explain the origin of the Galactic X-ray ridge (Valinia et al. 2000). This model was subsequently applied to G0.11−0.08 (Yusef-Zadeh et al. 2002). We argue below that this model can also be applied to Sgr C, as well as other Galactic center molecular clouds. In addition, we argue an alternative model to explain the origin of TeV emission from molecular clouds near the Galactic center. We suggest that the high-energy component of electrons can potentially be responsible for inverse Compton scattering the intense submillimeter emission to account for the origin of $\gamma$-ray emission.

### 4.1. *The Irradiation versus LECR Model*

One of the main results of our analysis of the millimeter and X-ray data is that the distributions of the 6.4 keV line and 2–6 keV continuum emission arise from the western edge of the $^{13}$CO molecular cloud. The main body of the Sgr C cloud does not show any evidence of X-ray emission except from its western edge, which faces away from the direction of Sgr A$^*$. The origin of fluorescent line emission resulting from irradiation by a hypothetical transient source associated with Sgr A$^*$ has been applied to the Galactic center molecular clouds (e.g., Sunyaev et al. 1993; Koyama et al. 1996; Murakami et al. 2001b; Park et al. 2004). However, unlike Sgr B2, the X-ray emission from Sgr C faces away from the suggested illuminating source, Sgr A$^*$. The column density of molecular hydrogen $10^{23}$–$10^{24}$ corresponds to Thompson optical depth $\tau_{\rm T}$ of 0.1–1 (Sunyaev & Churazov 1998). If the illuminating source is outside the cloud, the expected equivalent width exceeds 1 keV for an optically thin or thick case. The combined distribution of 6.4 keV line emission from Sgr C with respect to the bulk of molecular gas, as well as Sgr A$^*$ when combined with the estimated EW of $\sim$470 eV toward Sgr C, suggests strongly that the irradiation model is unlikely to be applicable to Sgr C.

We propose an alternative model to explain the origin of X-ray emission from Sgr C in terms of the impact of LECRs with molecular gas. The motivation for such a process stems from the fact that Sgr C is surrounded by a large concentration of nonthermal radio emission associated with radio filaments. Given that the centroids of X-ray and radio continuum features are displaced with respect to each other, it is remarkable that all of the X-ray continuum features, labeled in Figure 1*a*, appear to be located in the vicinity of peak nonthermal radio continuum emitting features associated with the Sgr C nonthermal filaments. Furthermore, the 6.4 keV line emission generally follows the X-ray continuum emission for almost all of the X-ray features with the exception of G359.32−0.16, which could be a pure nonthermal continuum source with no X-ray emission lines or molecular counterpart. The model proposed here can naturally explain the origin of hot molecular gas observed throughout the Galactic center molecular clouds.

In the context of the LECR model, the remarkable mixture of thermal and nonthermal radio components in Sgr C can produce not only the 6.4 keV line emission but also the nonthermal bremsstrahlung emission from Sgr C. As pointed out in § 2, the X-ray spectrum could be equally fitted by a combined soft thermal and a power-law spectrum as long as the metallicity is higher than the solar value. The power-law spectrum of the continuum emission from Sgr C is consistent with the LECR model, as described quantitatively below.

What about nonthermal filaments that have X-ray counterparts with no 6.4 keV counterpart? We believe that a flat spectrum of these filaments reduces the number of LECRs for interaction with molecular gas but increases the number of high-energy particles needed to produce synchrotron X-ray emission. The nonthermal X-ray filament discovered by Sakano et al. (2003) coincides exactly with a flat nonthermal radio source that is thought to be associated with "the 20 km s$^{-1}$ molecular cloud" (Ho et al. 1985; Coil & Ho 2000; Yusef-Zadeh et al. 2005). Assuming that this cloud is near the Galactic center, the lack of strong 6.4 keV and TeV emission from this molecular cloud could be explained by the flat spectrum of its nonthermal filament.

The source of the enhanced cosmic-ray electrons is acceleration at the interaction site between the Sgr C molecular cloud and the Sgr C nonthermal radio filaments. The distribution of diffuse and filamentary X-ray gas lying at the edge of the filaments implies the presence of relativistic electrons in the vicinity of the diffuse X-ray source. However, either the X-ray and radio features, as identified in Figures 1*a* and 3, are displaced from each other, or the X-ray features peak at the edge of nonthermal radio filaments. A displacement was also observed between the peak emission from radio filaments of the continuum arc and the M0.11−0.08 molecular cloud. The filaments of the arc and G0.11−0.08 are thought to be interacting with each other (Tsuboi et al. 1997; Oka et al. 2001). In addition, the LECR model has been successfully applied to this cloud (Yusef-Zadeh et al. 2002). Thus, the displacement of radio-emitting filaments and molecular cloud may be widespread in clouds that are interacting with nonthermal radio filaments. We believe that this characteristic can be explained by the geometry of the interacting nonthermal filaments with respect to the distribution of the molecular cloud. As described below, the low-energy relativistic particles interacting with neutral gas lose much more energy than the GeV particles that produce radio emission at high frequencies. The high-energy particles could be oblivious to the presence of molecular gas in their vicinity.

Interaction of cosmic rays with molecular gas has recently been argued to explain the origin of TeV emission from diffuse molecular gas. The gray-scale image in Figure 12 shows contours of TeV emission from the Galactic center region superimposed on a large-scale distribution of Fe K$\alpha$ line EW emission. There appears to be a correlation between the 6.4 keV EW line emission and TeV emission. The strongest TeV emission arises from the region near the arc, which is coincident with an EGRET source, as well as a soft $\gamma$-ray source 1743.1−2843 detected with *INTEGRAL* between 50 and 100 keV (Belanger et al. 2006). This source has been suggested to be produced as a result of the impact of GeV particles of the nonthermal filaments and G0.11−0.08 (Yusef-Zadeh et al. 2002). Whatever the mechanism responsible for the $\gamma$-ray emission from this source, it is suggestive that cosmic rays interacting with dense Galactic center molecular clouds are responsible for both types of X-ray, as well as soft and hard $\gamma$-ray, emission. Apart from supernova remnants and nonthermal filaments, massive stellar clusters can also provide relativistic particles generated as a result of wind-wind collision in a dense stellar cluster. The Arches cluster is one example that has shown a flux of $\sim$100 mJy of nonthermal emission from the cluster (Yusef-Zadeh et al. 2003).

### 4.2. *Injection of Cosmic Rays into Molecular Clouds*

We now calculate the production rate of Fe K$\alpha$ photons associated with the injection of $dn(E)/dt$ electrons per unit energy

interval per unit time into a cloud with column density $N_{\rm H}$. The column density of the Sgr C cloud in the vicinity of the X-ray emission is $N_{\rm H} \sim 10^{23}$ cm$^{-2}$. This is sufficient to stop electrons with energies below $\sim$1 MeV; the rapid increase in penetrating power with energy means that higher energies pass through this column with little fractional energy loss (see, e.g., ICRU 1984). Electrons with initial energy below a critical value $E_c(N_{\rm H})$ (1 MeV for $10^{23}$ cm$^{-2}$) are stopped in the cloud. A single electron injected with energy $E < E_c$ produces

$$z\omega_{\rm K} f_\alpha \int_0^E \sigma_{\rm K}(E') \frac{-dN_s}{dE'}\, dE' \quad (6)$$

Fe K$\alpha$ photons while coming to rest, where $z$ is the abundance of iron relative to hydrogen ($z_\odot = 2.8 \times 10^{-5}$), $\omega_{\rm K} = 0.342$ is the fraction of K-shell ionizations that produce K-characteristic X-rays, $f_\alpha = 0.822$ is the fraction of those that produce a K$\alpha$ photon, and $N_s(E)$ is the column density traversed by electrons of initial energy $E$ before coming to rest. In steady state the net K$\alpha$ production rate produced by the injected electrons with energies $E < E_c$ is therefore

$$Q_1 = z\omega_{\rm K} f_\alpha \int_0^{E_c} \frac{dn(E)}{dt} \int_0^E \sigma_{\rm K}(E') \frac{-dN_s}{dE'}\, dE'\, dE. \quad (7)$$

Reversing the order of integration yields

$$Q_1 = z\omega_{\rm K} f_\alpha \int_0^{E_c} \sigma_{\rm K}(E) \frac{-dN_s}{dE} \frac{dn}{dt} (E < E' < E_c)\, dE. \quad (8)$$

Electrons that enter the cloud at higher energies only lose a fraction of their energy; for simplicity we neglect this energy loss in calculating their contribution to the Fe K$\alpha$ production rate and write

$$Q_2 = z\omega_{\rm K} f_\alpha N_{\rm H} \int_{E_c}^\infty \frac{dn}{dt}(E)\sigma_{\rm K}(E)\, dE. \quad (9)$$

This "thin-target" approximation is adequate for our purposes here because $\sigma_{\rm K}$ varies by only a factor of 2 between 10 keV (e.g., Tatischeff 2003) and 1 GeV.

For $\sigma_{\rm K}(E)$ we use the semiempirical expression of Quarles (1976) with an ionization threshold energy $I = 7.1$ keV appropriate for neutral or almost neutral iron. The spectrum of injected electrons is assumed to be a power law ($E^{-p}$) between 10 keV and 1 GeV, normalized so that the corresponding power is 1 erg s$^{-1}$. The corresponding production rate $q = Q_1 + Q_2$ of Fe K$\alpha$ photons per erg of injected electron energy is calculated using equations (8) and (9) as a function of cloud column density.

The results are plotted in Figure 13*a* for electron spectral indices $p$ ranging from 2 to 3 and a solar iron abundance. For a given particle spectral index $p$, the efficiency of K$\alpha$ production increases with column density, eventually flattening when the column is sufficient to stop the bulk of the injected electrons within the cloud. For the $p = 2$ injection spectrum, which has equal energy per decade between 10 keV and 1 GeV, this occurs above $10^{25}$ cm$^{-2}$, which can only stop electrons with energies below 0.1 GeV. Steeper spectra have particle energies increasingly concentrated toward 10 keV and so the flattening of the K$\alpha$ production rate occurs at successively lower column densities. These results are consistent with those of Tatischeff (2003), who found

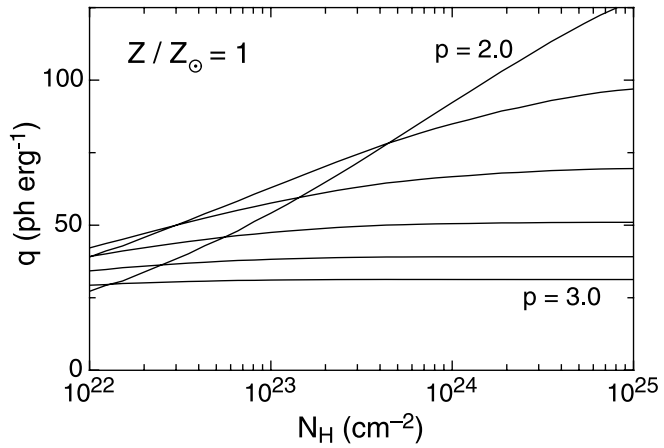


FIG. 13*a*

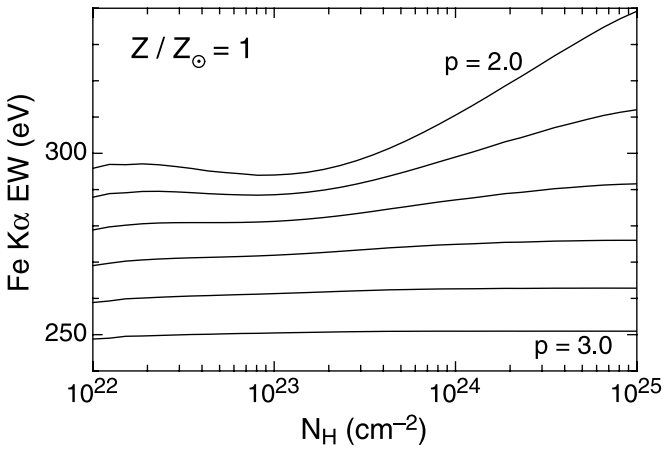


FIG. 13*b*

FIG. 13.—(*a*) Fe K$\alpha$ production per erg of electron energy injected into a cloud of given column density $N_{\rm H}$ and a solar iron abundance (Fe/H $= 2.8 \times 10^{-5}$). The lines are labeled by the power-law index $p$ of the electron energy spectrum ($\propto E^{-p}$), which is assumed to run from 10 keV to 1 GeV. (*b*) Similar to (*a*), except that the equivalent width of Fe K$\alpha$ is shown as a function of column density for different values of the particle spectral index.

$q \sim 50$ photons erg$^{-1}$ for 10–100 keV electrons with an $E^{-2}$ spectrum. We conclude from Figure 13*a* that typically $q \sim 50 z/z_\odot$ photons erg$^{-1}$ for typical spectral indices and cloud column densities, increasing to $\sim 100 z/z_\odot$ for hard electron spectra and high column densities. The bremsstrahlung emission at 6.4 keV was estimated similarly; the resulting equivalent width is plotted in Figure 13*b*. For $z = z_\odot$, the equivalent width varies between 250 and 300 eV for particle spectral index $p$ varying between 3 and 2. There is little dependence on column except for $p$ close to 2 and columns in excess of $10^{24}$ cm$^{-2}$, where the equivalent width increases from 300 to 340 eV as the column increases toward $10^{25}$ cm$^{-2}$. The Galactic center molecular clouds have typical metallicity that is on the average twice the solar value (e.g., Giveon et al. 2002; Rudolph et al. 2006). Thus, the production of K$\alpha$ line emission per erg of energy and the EW of K$\alpha$ emission, as shown in Figure 13, should be increased by a factor of 2 when applied to the Galactic center molecular clouds.

### 4.3. *Application of the Low-Energy Cosmic-Ray Model*

To estimate the flux of electrons into the cloud, we assume that they diffuse from their acceleration site to the cloud edge and then freely stream into the cloud because ion-neutral damping

TABLE 3
PARAMETERS OF THE LECR MODEL

| Region | Area (arcmin$^2$) | 90 cm Flux (Jy) | Energy Density (eV cm$^{-3}$) | Magnetic Field (mG) | Spectral Index $\alpha$ |
|---|---|---|---|---|---|
| Sgr C | 0.024 | 0.05 | 1200 | 0.22 | $-0.7$ |
| Radio arc | 285 | 260 | 19 | 0.029 | 0.0 |
| Arches cluster | 1.6 | 0.36 | $6 \times 10^4$ | 1.6 | $-1$ |
| Sgr B1 | 77 | 3.2 | 23 | 0.03 | $-0.7$ |
| Sgr B2 | 96 | 18 | 51 | 0.045 | $-0.7$ |

suppresses the magnetic fluctuations responsible for the diffusion. If the energy density of the electrons external to the cloud is $U$, then the flux into the cloud is $\sim cU/4$, giving an injection rate $cUA/4$, where $A \sim \Omega d^2$ is the cloud surface area impinged on by electrons, $\Omega$ is the solid angle of the X-ray emission, and $d$ is the distance to the cloud from the Earth. The production rate of Fe K$\alpha$ photons is $Q \approx cU\Omega d^2 q/4$. The intensity of Fe K$\alpha$ photons at the Earth is then

$$I_{\mathrm{K}\alpha} = \frac{Q}{4\pi d^2 \Omega} = \frac{cUq}{16\pi} \approx 8 \times 10^{-6} \left( \frac{U}{10^3 \text{ eV cm}^{-3}} \right) \times \left( \frac{z}{2z_\odot} \right) \text{ photons s}^{-1} \text{ cm}^{-2} \text{ arcmin}^{-2}, \quad (10)$$

comparable to the observed peak Fe K$\alpha$ intensities if $U \sim 1000$ eV cm$^{-3}$.

We apply this model to some of the sources in the Galactic center region. In each case we assume that the nonthermal radio emission is produced by a power-law spectrum $n(E) \propto E^{-p}$ of electron energies between 10 keV and 1 GeV, assume that the depth of the emitting region is of the order of its diameter, and calculate the energy density of cosmic-ray electrons assuming that they are in equipartition with the magnetic field. Equation (10) is then used to compute the predicted Fe K$\alpha$ flux; when the source of particles is either assumed to be embedded within the cloud or completely surrounds it, this estimate is increased by a factor of 4 to allow for the increase in exposed surface area exposed to the incident cosmic rays (i.e., $4\pi r^2$ rather than $\pi r^2$). Note that although the incident electron spectrum may deviate from a power law below 100 keV because of ionization losses, this is not a major uncertainty as these electrons contribute $\lesssim$20% of the K$\alpha$ flux. The model parameters needed to match the observed quantities for each source are listed in Table 3.

#### 4.3.1. *Sgr C*

The brightest filament associated with Sgr C has a typical synchrotron flux at 90 cm of 50 mJy per $12.6'' \times 6.8''$ beam with a $\nu^{-0.7}$ spectrum. This is a lower limit to the flux of synchrotron emission because diffuse synchrotron emission, free-free absorption by intervening thermal gas, and contribution from weak nonthermal filaments have not been accounted for. The equipartition field is 0.22 mG with an electron energy density of 1200 eV cm$^{-3}$. This implies a peak K$\alpha$ flux of $9.7 \times 10^{-6}$ photons cm$^{-2}$ arcmin$^{-2}$, which is about 1.5 times that observed. We have used a particle spectral index $p = 2.4$ [where $n(E) \propto E^{-p}$] and equipartition between electrons and magnetic field. The measured spectral index values between 90 and 20 cm wavelengths agree well with the energy density in relativistic electrons required to match the synchrotron emission.

#### 4.3.2. *The 45 and $-30$ km s$^{-1}$ Clouds near the Radio Arc*

The filaments of the radio arc have a flux of $\sim$28 Jy at 90 cm over its $3' \times 20'$ area, with a $\nu^{-0.5}$ spectrum. This spectrum is consistent with that measured between 408 and 160 MHz (Yusef-Zadeh et al. 1986). Most of the diffuse nonthermal emission is likely to be resolved out, so we used the Green Bank observations of this region (Law 2007) and measured a total integrated flux of 200 Jy over 285 arcmin$^2$. This region includes the linear filaments of radio arc and other weaker nonthermal filaments that have recently been discovered (Reich 2003; Yusef-Zadeh et al. 2004; Nord et al. 2004) within the area of the extracted X-ray spectrum (Fig. 11 and the box area in Fig. 2). Due to the contamination by thermal H II features, as well as the background emission at 90 cm, the flux of nonthermal emission has a large uncertainty. Using the recent 20 cm continuum image, which includes the zero spacing flux (Yusef-Zadeh et al. 2004), we found a similar flux of about 200 Jy, which is consistent with the 90 cm measurements having a flat spectral index between 20 and 90 cm (Yusef-Zadeh et al. 1986).

Adopting 28 Jy of flux density of the nonthermal filaments of the arc at 90 cm and assuming that the arc consists of filaments of thickness $30''$, the equipartition field is 0.07 mG and the energy density of electrons is 110 eV cm$^{-3}$. The predicted K$\alpha$ flux, $4 \times 10^{-5}$ photons cm$^{-2}$ s$^{-1}$, is much lower than that measured ($3.5 \times 10^{-4}$ photons cm$^{-2}$ s$^{-1}$). If we assume instead that the source is embedded in a diffuse distribution of LECR electrons over 285 arcmin$^2$ with a source depth of $15'$, then we find that an energy density of 38 eV cm$^{-3}$ is required, with field strength 0.039 mG and synchrotron flux of 860 Jy. If the column density of the clouds is $\sim 10^{24}$ cm$^{-2}$ and $p \sim 2$, then $q$ increases to $100 z/z_\odot$ photons erg$^{-1}$; the required energy density, field strength, and diffuse synchrotron flux are reduced to 19 eV cm$^{-3}$, 0.0289 mG, and 260 Jy, respectively.

#### 4.3.3. *The Arches Cluster*

As discussed in § 3.2, we found a knotlike K$\alpha$ emission in the vicinity of the Arches cluster. The source of cosmic-ray particles injecting into the cloud surrounding the Arches cluster can either be the nonthermal filaments of the arc or nonthermal particles generated by the cluster. Figure 14 shows a detailed view of the Arches cluster that coincides with a compact nonthermal radio continuum source (*black*) at 90 cm (Yusef-Zadeh et al. 2003) against the gray-scale distribution of the EW of 6.4 keV line emission. An X-ray spectrum was extracted from the region shown in Figure 14 that roughly encloses the 600 eV contours. The extracted region, as shown in Figure 2, is defined by an ellipse centered on $l = 7'33.7''$, $b = 1'08.6''$ having a major and minor axis of $62.7''$ and $29.1''$ (P.A. $= 25^\circ$), respectively. The parameters of

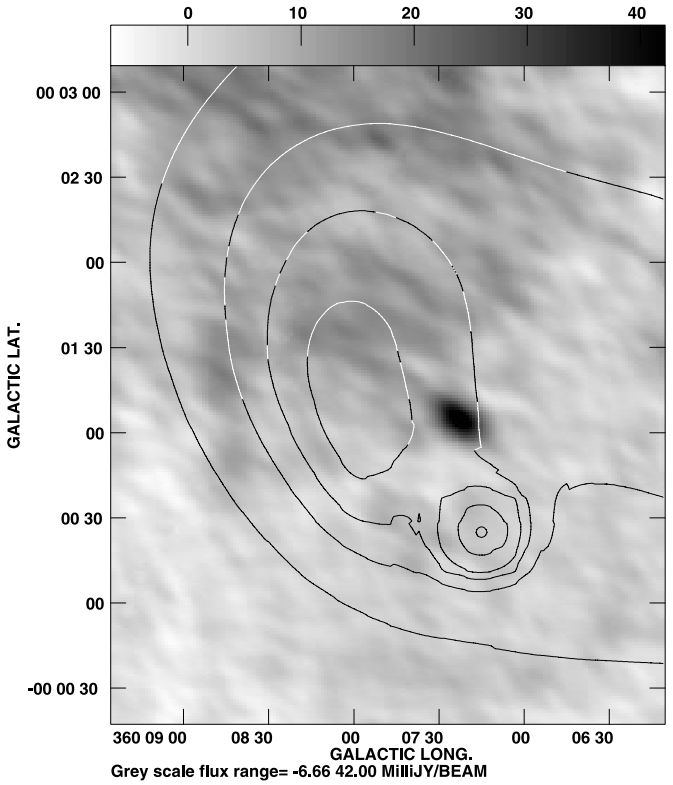


FIG. 14.—Contours of EW of Fe K$\alpha$ line emission with levels (3, 4, 5, 6, 8, 10) $\times$ 100 eV superimposed on a gray-scale distribution of 90 cm emission from the Arches cluster (*black*).

the iron line emission are shown in Table 2, having Fe K$\alpha$ EW of 810 eV. The peak EW emission in Figure 14 is as much as 1000 eV.

The nonthermal 327 MHz flux from the Arches cluster is 91 mJy over a 7″ by 13.5″ region (Yusef-Zadeh et al. 2002), with a spectral index $\alpha \approx 1$ (for $S\nu \propto \nu^{-\alpha}$). The equipartition magnetic field is 1.1 mG and the energy density of electrons is $3 \times 10^4$ eV cm$^{-3}$. The predicted K$\alpha$ flux, $6.5 \times 10^{-6}$ photons cm$^{-2}$ s$^{-1}$, agrees with that observed by Wang et al. (2006), i.e., $6.2 \times 10^{-6}$ photons cm$^{-2}$ s$^{-1}$. However, if we use the integrated K$\alpha$ flux from the region shown in Figure 14 and Table 2, the required 90 cm flux increases to 360 mJy of nonthermal emission from the Arches cluster with an equipartition magnetic field of 1.6 mG. The additional flux of nonthermal emission must arise from the diffuse nonthermal emission surrounding the cluster or the emission from the nonthermal filaments of the arc.

#### 4.3.4. *Sgr B2 and Sgr B1*

Radio continuum observations of the Sgr B complex show two major components, Sgr B1 (G0.5−0.0) and Sgr B2 (G0.7−0.0), as well as an intervening source G0.6−0.0 in the middle of these extended H II regions (e.g., Mehringer et al. 1992). Diffuse thermal emission dominates Sgr B1, whereas numerous ultracompact H II regions overwhelm the emission in Sgr B2.

The continuum emission from Sgr B2 is mainly due to several dozen ultracompact H II regions, and there is no known source of nonthermal filaments in its vicinity. However, there is a bright compact radio source detected at 90 cm with a flux density of 112 mJy at $l = 40'2.1''$, $b = -2'7''$ detected at 90 cm (Nord et al. 2004). This source is likely to be nonthermal due to colliding winds from binary systems similar to the bright nonthermal source in the Arches cluster (F. Yusef-Zadeh et al. 2007, in preparation). If we assume that this central nonthermal radio source has a size about $10'' \times 10''$ with a $\nu^{-0.7}$ spectrum, the equipartition field is 0.36 mG with an estimated electron energy density of 2500 eV cm$^{-3}$. This also yields an estimated flux of $3.3 \times 10^{-6}$ photons cm$^{-2}$ s$^{-1}$ assuming $q = 150$ photons erg$^{-1}$. In light of its large column density and including a factor of 4 leakage from the nonthermal source because it is entirely enclosed within the molecular cloud (so the relevant surface area is $4\pi r^2$ rather than $\pi r^2$), the predicted flux is still 50 times lower than observed. Another difficulty is that the strength of the equivalent width of K$\alpha$ line emission is roughly 2 times higher than other Galactic center clouds with the exception of the Arches cluster.

Thus, the lack of strong localized nonthermal emission (unlike other Galactic center molecular clouds) makes it difficult to apply the LECR picture to Sgr B2. However, the strong three-way correlation between the distribution of molecular clouds, the K$\alpha$ line emission, and TeV emission from the Galactic center clouds suggests that the same process should be able to explain these observations. Adopting a size of 96 arcmin$^2$, source depth 10′, and a $\nu^{-0.7}$ spectrum, the required electron energy density, equipartition field, and resulting 90 cm synchrotron flux are 51 eV cm$^{-3}$, 0.045 mG, and 18 Jy, respectively. Observationally, there may be diffuse nonthermal emission surrounding the Sgr B2 cloud. Figure 15*a* shows a low-resolution VLA continuum image of Sgr B2 at 90 cm with FWHM $= 41.6'' \times 22.7''$ against contours of EW K$\alpha$ line emission. The integrated flux at 90 cm is about 17 Jy, which is likely to be mainly due to thermal emission from H II regions. It is difficult to disentangle nonthermal from thermal emission from this region. There is also a degree-scale diffuse feature surrounding Sgr B2 based on Green Bank observations at 90 cm (C. Law et al. 2007, in preparation). However, it is not clear how much of this large-scale diffuse emission, which is more than sufficient to account for the origin of 6.4 keV emission, arises from Sgr B2. The total background-subtracted integrated 90 cm flux from the region covering Sgr A, B, C and the continuum arc is about ∼1200 Jy, most of which is expected to be nonthermal.

The large EW of Fe K$\alpha$ line emission in Sgr B2 may result from the high abundance of iron by roughly a factor of 3–4 times the solar value. Other parameters that could increase the strength of EW are column density and the spectrum of the nonthermal emission, neither of which can be important as shown in Figures 13*a* and 13*b*. The Galactic center molecular clouds show metallicity that is generally twice as high as in the solar neighborhood; thus, we are predicting that Sgr B2 could have a 1.5–2 times higher metallicity than that of typical Galactic center clouds.

Sgr B1 lies adjacent to a number of nonthermal radio filaments with flux densities of ∼10 mJy on the eastern side of the Sgr B1 cloud; Figure 15*b* shows the contour distribution of EW of K$\alpha$ emission against the gray-scale 90 cm image. The prominent nonthermal filaments observed at 90 cm clearly show their distribution with respect to the edge of K$\alpha$ line emission. The integrated 90 cm flux from the filaments shown in Figure 15*b* is roughly 800 mJy. The distribution of EW over the region of Sgr B1 shown in Figure 2 ranges between a few hundred to 1500 eV near $l = 34'7''$, $b = -1'13''$. The extracted spectrum over this region gives EW ∼ 570 eV (Table 2). Adopting a size of 77 arcmin$^2$, source depth 10′, and a $\nu^{-0.7}$ spectrum, the required electron energy density, equipartition field, and resulting 90 cm synchrotron flux are 23 eV cm$^{-3}$, 0.030 mG, and 3.2 Jy, respectively.

### 4.4. *Cosmic-Ray Heating of Molecular Clouds*

The heating associated with the electron energy losses is significant. It is dominated by the electrons entering the cloud with initial energies between 0.1 and 1 MeV as lower energy electrons are injected less efficiently, and higher energy electrons do not

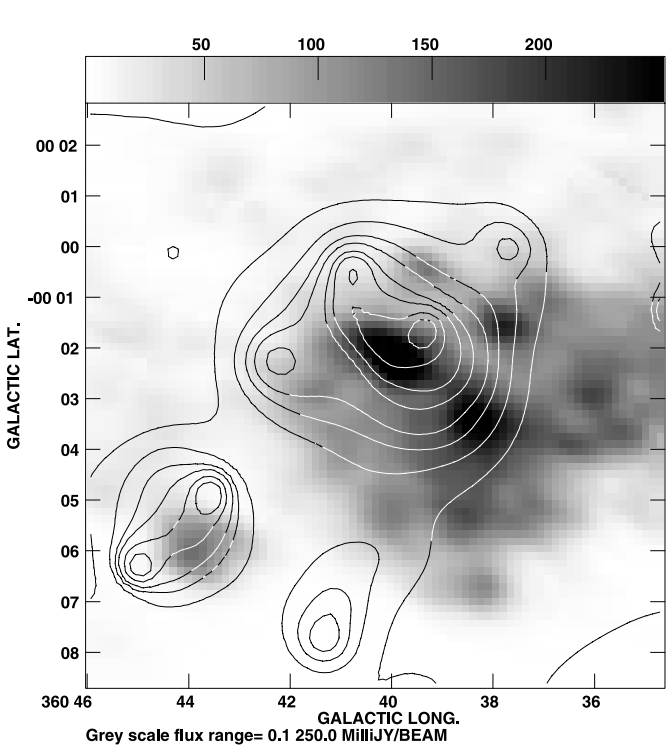


FIG. 15*a*

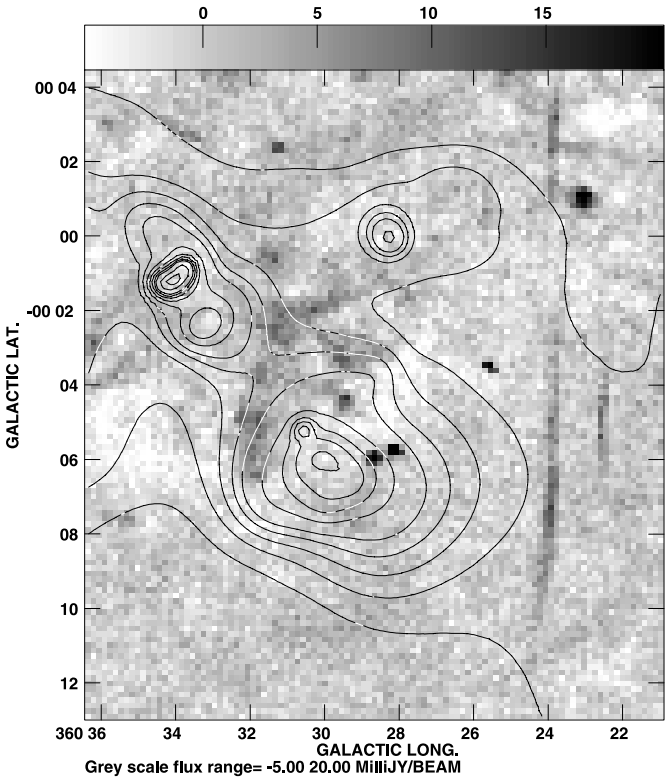


FIG. 15*b*

FIG. 15.—(*a*) Contours of EW of Fe K$\alpha$ line emission from Sgr B2 with levels (1, 2, 3, 4, 5, 6, 8, 10, 14, 18, 22) $\times$ 100 eV superimposed on a gray-scale distribution of 90 cm emission from Sgr B2 with a resolution of $41.7'' \times 22.7''$ (P.A. $= -6^\circ$; Anantharamaiah et al. 1991). (*b*) Contours of EW of Fe K$\alpha$ line emission from Sgr B1 with levels (1, 1.5, 2, 2.5, 3, 4, 5, 6, 7, 8, 11, 14) $\times$ 100 eV superimposed on a gray-scale distribution of 90 cm emission from Sgr B1 and G0.6$-$0.0 in black color with a resolution of $12.6'' \times 6.8''$ (P.A. $= 3^\circ$).

lose much of their energy in the cloud. For each erg of electron energy deposited into the cloud, approximately 10% goes into heat (Dalgarno et al. 1999) and 200 Fe K$\alpha$ photons are produced; thus, the heating rate is

$$\frac{\Gamma}{n_{\rm H}} = 0.1 \frac{4\pi I_{\rm K\alpha}}{N_{\rm H}} \frac{2/3}{200 \text{ photons erg}^{-1}} \sim 3 \times 10^{-24} \text{ ergs s}^{-1} \text{ H}^{-1}, \quad (11)$$

where the factor of $\frac{2}{3}$ removes the contribution of $E > 10$ MeV electrons to $I_{\rm K\alpha}$. This heating rate implies temperatures of $\sim$200 K for $n({\rm H_2}) \sim 1 \times 10^4$ cm$^3$ and $N_{\rm H_2}/\Delta v \sim 10^{22}$ cm$^{-2}$ km$^{-1}$ s (Neufeld et al. 1995). Such a high temperature due to LECR heating is consistent with multitransition ammonia line observations indicating a warm 200 K gas observed throughout the Galactic center region (e.g., Hüttemeister et al. 1993a; Rodriguez-Fernandez et al. 2004; Oka et al. 2005). There is also a denser and colder component of molecular gas that has been detected to have small volume filling factor. If the denser component lies in the Galactic center, we believe that either cosmic rays have not penetrated these dense regions or the higher cooling rate of dense gas has lowered the gas temperature.

### 4.5. *Cosmic-Ray Ionization Rate in the Galactic Center*

We can also estimate that the ionization of the molecular gas is associated with the losses of electrons with incident energies between 0.1 and 1 MeV. The ionization rate is readily estimated from equation (11) by noting that, on average, an ionization occurs for each deposition of 40.1 eV of electron energy into the gas (Dalgarno et al. 1999), yielding $\zeta \approx (3 \times 10^{-24}$ ergs s$^{-1}$ H$^{-1}$)/(40.1 eV) $\approx 5 \times 10^{-13}$ s$^{-1}$ H$^{-1}$. This value of $\zeta$ is about 4 orders of magnitude higher than the canonical value of the interstellar cosmic-ray ionization rate and corresponds to an energetic electron energy density of $\sim$1000 eV cm$^{-3}$, appropriate for Sgr C. This is reduced by 1–2 orders of magnitude for Sgr B1 and B2 and the radio arc (see Table 3), giving $\zeta \sim 2 \times 10^{-14}$ s$^{-1}$ H$^{-1}$ for these sources. As pointed out earlier, the detection of a substantial amount of the (3, 3) metastable rotational levels of $H3^+$ in the Galactic center region requires an estimated high ionization rate, which is estimated to be about 2 orders of magnitude higher than that for diffuse clouds (Oka et al. 2005). Thus, cosmic rays in the Galactic center region may be responsible for producing the large reservoir of warm molecular gas that is inferred from $H3^+$ measurements.

## 5. THE ORIGIN OF DIFFUSE TeV EMISSION

Inverse Compton scattering (ICS) of the submillimeter radiation from dust in the Galactic center clouds by relativistic electrons may account for or significantly contribute to the diffuse TeV emission observed toward the central regions of the Galaxy (Aharonian et al. 2006). For example, the strongest HESS peak overlays the arc (see Fig. 12). To estimate this contribution, we assume that the dust emission in the region is isotropic with intensity $I_\nu = B_\nu(T_d)[1 - \exp(-\tau_d)]$, where $T_d = 20$ K is the dust temperature and the dust optical depth $\tau_d \propto \nu^2$ (Pierce-Price et al. 2000). The 850 and 400 $\mu$m SCUBA maps yield an estimate of $\tau_d = 0.029$ at $\nu = kT_d/h$. The electron spectrum associated with the arc must extend

to at least 30 TeV to produce upscattered photons at TeV energies. An extrapolation of the $E^{-2}$ electron spectrum that obtains at GeV energies into the TeV range predicts a photon flux at 1 TeV that is 60 times that observed, which we estimate to be $\sim 1 \times 10^{-13}$ photons cm$^{-2}$ s$^{-1}$ (Aharonian et al. 2006). However, one expects a synchrotron break at lower energies, and the observed TeV spectrum has a photon index of roughly $-2.3$, steeper than the $-1.5$ this simple model would predict. Instead, we assume that synchrotron losses steepen the electron spectrum at energies above 2 TeV to an $E^{-3}$ dependence; the corresponding synchrotron loss timescale is 1000 yr. This steepens the predicted ICS photon spectrum from $E_\gamma^{-1.5}$ to $E_\gamma^{-2}$ above 40 GeV and matches the observed HESS flux at 1 TeV.

## 6. CONCLUSIONS

The distributions of $^{13}$CO line, X-ray, nonthermal radio continuum, and 6.4 keV line emission suggest against the irradiation origin of X-ray emission from Sgr C. We believe that the origin of X-ray continuum and line emission can naturally be explained by the interaction of cosmic rays with prominent Galactic center molecular clouds such as Sgr C, the 45 and $-30$ km s$^{-1}$ clouds, Sgr B1, and Sgr B2. We have argued that the sources of nonthermal particles are due to a combination of the Galactic center radio filaments that are localized in the immediate vicinity of molecular clouds and the diffuse nonthermal component distributed throughout the Galactic center region. This hypothesis is consistent with the similar value of 6.4 keV equivalent width throughout the Sgr C, the $-30$ and 45 km s$^{-1}$ clouds near the radio arc, and Sgr B1 regions.

In the context of this model, we explain the high value of the equivalent width of Fe K$\alpha$ line and unusually strong K$\alpha$ line emission from Sgr B2 in terms of higher metallicity and the contribution of diffuse nonthermal particles in this source. The interaction of the nonthermal radio filaments and the molecular cloud implies that these features are at the same distance from each other and that the long-standing problem of the origin of high-temperature molecular gas can naturally be explained in terms of the LECR heating of the clouds. In addition, we estimate the high cosmic-ray ionization rate in the Galactic center region, which could explain the origin of warm molecular gas as traced by $H_3^+$ absorption study. In addition, we provide an alternative model to explain the origin of diffuse TeV emission from molecular clouds in the central region of the Galaxy by using the high-energy component of nonthermal electrons to upscatter the submillimeter emission from dust clouds in this region. The remarkable correlation of K$\alpha$ line emission, TeV emission, and molecular gas suggests that similar processes are at work in explaining both diffuse X-ray and $\gamma$-ray emission from the Galactic center clouds. Lastly, we believe that the interplay between the cosmic rays and neutral gas in the central region of the Galaxy is significant and provides much insight into our understanding of the physical processes that are involved in both the nuclei and the disks of galaxies.

We are grateful to J. Hinton, N. Kassim, D. Pierce-Price, and Y. Tsuboi for providing us with their published data. D. C. L. is supported by NSF grant AST 05-40882 to Caltech Submillimeter Observatory.

## APPENDIX

## POLARIZATION MEASUREMENTS

Additional support for the synchrotron nature of the filament comes from polarization measurements. We carried out a high-frequency polarization study of Sgr C at 3.6 cm to reduce the effect of Faraday rotation toward this source. Figure 10*a* shows a gray-scale image of linearly polarized emission from the linear filament of Sgr C with line segments indicating the polarization angle distribution at 3.6 cm. The peak emission has a flux density of 1.4 mJy beam$^{-1}$ near the center of the image and $\sim$0.28 mJy beam$^{-1}$ away from the center. The degree of polarization is remarkably high, corresponding to a value of about 65%. In contrast, in the region to the south of this highly polarized feature, the polarization degree drops off to 10% near the compact source G359.45$-$0.05. The low degree of linear polarization to the south of the filament could be due to the contamination by the bright thermal emission from the Sgr C H II region. This diffuse H II region is likely responsible for depolarization of synchrotron emission from the Sgr C filaments. Due to high Faraday rotation toward the Galactic center sources, we are not able to determine the intrinsic direction of the magnetic field along the Sgr C filament. Assuming that depolarization is caused by an external medium, the lack of strong polarized emission to the south suggests that the filament either lies behind the H II region or is embedded within it.

Figure 10*b* shows a gray-scale image of Sgr C at 3.6 cm with a resolution $9.8'' \times 7.5''$ (P.A. $= -7.5^\circ$). We note several circular-like extended features to the north and south of the Sgr C filament, as well as a bright compact source along the filament. These features generally show a flatter spectrum than the linear filament. The compact source G359.45$-$0.05 ($l = 359^\circ 27' 19.94'' \pm 0.002$, $b = -03' 22.49'' \pm 0.04$) has a spectral index of roughly $-0.29 \pm 0.21$ between 3.6 and 2 cm. Other extended sources are identified as G359.45$-$0.07, G359.45$-$0.03, and G359.45$-$0.02 in Figure 9, all of which appear to be thermal sources having mean spectral index values $\alpha = -0.1 \pm 0.24$, $-0.09 \pm 0.3$, and $-0.02 \pm 0.3$, respectively. It is difficult to determine the true relationship between these features and the nonthermal filament with the available resolution, especially in the case of the ring-shaped morphology of G359.45$-$0.07, in which the nonthermal filament appears to pass through the ring, and in the case of the compact source G359.45$-$0.5. We also note a weak vertical filament to the south of the Sgr C H II region directed south of Galactic latitude $b = -6'$, as shown in Figure 10*b*. This feature needs to be confirmed as it falls outside the primary beam of our 3.6 cm image and has never been detected in previous radio continuum images of Sgr C.

## REFERENCES

Aharonian, F., et al. 2006, Nature, 439, 695
Anantharamaiah, K. R., Pedlar, A., Ekers, R. D., & Goss, W. M. 1991, MNRAS, 249, 262
Anantharamaiah, K. R., & Yusef-Zadeh, F. 1989, in IAU Symp. 136., The Center of the Galaxy, ed. M. Morris (Dordrecht: Kluwer), 159
Arnaud, K. A. 1996, in ASP Conf. Ser. 101, Astronomical Data Analysis Software and Systems V, ed. G. Jacoby & J. Barnes (San Francisco: ASP), 17
Belanger, G., et al. 2006, ApJ, 636, 275
Boldyrev, S., & Yusef-Zadeh, F. 2006, ApJ, 637, L101
Caswell, J. L., & Haynes, R. F. 1987, A&A, 171, 261
Coil, A., & Ho, P. T. P. 2000, ApJ, 533, 245
Cotera, A., Erickson, E., Colgan, S., Simpson, J., Allen, D., & Burton, M. 1996, ApJ, 461, 750
Dalgarno, A., Yan, M., & Liu, W. H. 1999, ApJS, 125, 237

Downes, D., Goss, W. M., Schwarz, U. J., & Wouterloot, J. G. A. 1979, A&AS, 35, 1
Ekers, R. D., van Gorkom, J. H., Schwarz, U. J., & Goss, W. M. 1983, A&A, 122, 143
Erickson, N. R., Goldsmith, P. F., Novak, G., Grosslein, R. M., Viscuso, P. J., Erickson, R. B., & Predmore, C. R. 1992, IEEE Trans. Microwave Theory Tech., 40, 1
Figer, D. F., Sungsoo, S. K., Morris, M., Serabyn, E., Rich, R. M., & McLean, I. S. 1999, ApJ, 525, 750
Frerking, M. A., Langer, W. D., & Wilson, R. W. 1982, ApJ, 262, 590
Fryer, C. L., Rockefeller, G., Hungerford, A., & Melia, F. 2006, ApJ, 638, 786
Giveon, U., Morisset, C., & Sternberg, A. 2002, A&A, 392, 501
Gray, A. D. 1994, MNRAS, 270, 861
Güsten, R., Walmsley, C. M., & Pauls, T. 1981, A&A, 103, 197
Handa, T., Sakano, M., Naito, S., & Hiramatsu, M. 2006, ApJ, 636, 261
Helfand, D. J., & Becker, R. H. 1987, ApJ, 314, 203
Ho, P. T. P., Jackson, J. M., Barrett, A. H., & Armstrong, J. T. 1985, ApJ, 288, 575
Hüttemeister, S., Wilson, T. L., Banina, T. M., & Martin-Pintado, J. 1993a, A&A, 280, 255
Hüttemeister, S., Wilson, T. L., Henkel, C., & Mauserberger, R. 1993b, A&A, 276, 445
ICRU 1984, Stopping Powers for Electrons and Positrons (ICRU Rept. 37; Bethesda: ICRU)
Kassim, N. E., & Frail, D. A. 1996, MNRAS, 283, L51
Koyama, K., et al. 1996, PASJ, 48, 249
Lang, C. C., Goss, W. M., & Morris, M. 2002, AJ, 124, 2677
Lang, C. C., Morris, M., & Echevarria, L. 1999, ApJ, 526, 727
LaRosa, T. N., Brogan, C. L., Shore, S. N., Lazio, T. J., Kassim, N. E., & Nord, M. E. 2005, ApJ, 626, L23
Law, C. 2007, Ph.D. thesis, Northwestern Univ.
Law, C., & Yusef-Zadeh, F. 2004, ApJ, 611, 858
Lis, D. C., & Carlstrom, J. E. 1994, ApJ, 424, 189
Lis, D. C., & Goldsmith, P. F. 1989, ApJ, 337, 704
———. 1991, ApJ, 369, 157
Liszt, H. S. 1992, ApJS, 82, 495
Liszt, H. S., & Spiker, R. W. 1995, ApJS, 98, 259
Lu, F. G., Wang, Q. D., & Lang, C. C. 2003, AJ, 126, 319
Mehringer, D. M., Yusef-Zadeh, F., Palmer, P., & Goss, W. M. 1992, ApJ, 401, 168
Morris, M., & Serabyn, E. 1996, ARA&A, 34, 645
Muno, M. P., Bauer, F. E., Bandyopadhyay, R. M., & Wang, Q. D. 2006, ApJS, 165, 173
Muno, M. P., et al. 2004a, ApJ, 613, 326
———. 2004b, ApJ, 613, 1179
Murakami, H., Koyama, K., & Maeda, Y. 2001a, ApJ, 558, 687
Murakami, H., Koyama, K., Sakano, M., Tsujimoto, M., & Maeda, Y. 2000, ApJ, 534, 283
Murakami, H., Koyama, K., Tsujimoto, M., & Maeda, Y. 2001b, ApJ, 550, 297
Neufeld, D. A., Lepp, S., & Melnick, G. J. 1995, ApJS, 100, 132
Nord, M. E., Lazio, T. J. W., Kassim, N. E., Hyman, S. J., LaRosa, T. N., Brogan, C. L., & Duric, N. 2004, AJ, 128, 1646
Odenwald, S. F., & Fazio, G. G. 1984, ApJ, 283, 601
Oka, T., Geballe, T. R., Gotto, M., Usida, T., & McCall, B. 2005, ApJ, 632, 882
Oka, T., Hasegawa, T., Sato, F., Tsuboi, M., & Miyazaki, A. 2001, PASJ, 53, 779
Park, S., Baganoff, F. K., Morris, M., Maeda, Y., Muno, M. P., Howard, C., Bautz, M. W., & Garmire, G. P. 2004, ApJ, 603, 548
Pierce-Price, D., et al. 2000, ApJ, 545, L121
Quarles, C. A. 1976, Phys. Rev. A, 13, 1278
Reich, W. 2003, A&A, 401, 1023
Revnivtsev, M. G., et al. 2004, A&A, 425, L49
Rodriguez-Fernandez, N. J., Martin-Pintado, J., Fuente, A., de Vicente, P., Wilson, T. L., & Hüttemeister, S. 2001, A&A, 365, 174
Rodriguez-Fernandez, N. J., Martin-Pintado, J., Fuente, A., & Wilson, T. L. 2004, A&A, 427, 217
Roy, S. 2003, A&A, 403, 917
Rudolph, A. L., Fich, M., Bell, G. R., Norsen, T., Simpson, J. P., Haas, M. R., & Erickson, E. F. 2006, ApJS, 162, 346
Sakano, M., Warwick, R. S., Decourchelle, A., & Predhel, P. 2003, MNRAS, 340, 747
Serabyn, E., & Güsten, R. 1987, A&A, 184, 133
Sunyaev, R., & Churazov, E. 1998, MNRAS, 297, 1279
Sunyaev, R. A., Markevitch, M., & Pavlinsky, M. 1993, ApJ, 407, 606
Tatischeff, V. 2003, in Final Stages of Stellar Evolution, ed. C. Motch & J.-M. Hameury (Les Ulis Cedex: EAS), 79
Townsley, L. K., et al. 2002, Nucl. Instrum. Methods Phys. Res. A, 486, 751
Tsuboi, M., Handa, T., & Ukita, N. 1999, ApJS, 120, 1
Tsuboi, M., Kobayashi, H., Ishiguro, M., & Murata, Y. 1991, PASJ, 43, L27
Tsuboi, M. M., Ukita, N., & Handa, T. 1997, ApJ, 481, 263
Valinia, A., Tatischeff, V., Arnaud, K., Ebisawa, K., & Ramaty, R. 2000, ApJ, 543, 733
van der Tak, F. F. S., Belloche, A., Schilke, P., Güsten, R., Philipp, S., Comito, C., Bergman, P., & Nyman, L.-Å. 2006, A&A, 454, L99
Wang, Q. D., Dong, H., & Lang, C. 2006, MNRAS, 371, 38
Wang, Q. D., Gotthelf, E. V., & Lang, C. C. 2002, Nature, 415, 148
Weisskopf, M. C., Brinkman, B., Canizares, C., Garmire, G., Murray, S., & van Speybroeck, L. P. 2002, PASP, 114, 1
Wilson, T. L., & Rood, R. 1994, ARA&A, 32, 191
Yusef-Zadeh, F. 1986, Ph.D. thesis, Columbia Univ.
———. 2003, ApJ, 598, 325
Yusef-Zadeh, F., Hewitt, J. W., & Cotton, W. 2004, ApJS, 155, 421
Yusef-Zadeh, F., Law, C., & Wardle, M. 2002, ApJ, 568, L121
Yusef-Zadeh, F., Morris, M., & Chance, D. 1984, Nature, 310, 557
Yusef-Zadeh, F., Morris, M., Slee, O. B., & Nelson, G. J. 1986, ApJ, 310, 689
Yusef-Zadeh, F., Nord, M., Wardle, M., Law, C., Lang, C., & Lazio, T. J. W. 2003, ApJ, 590, L103
Yusef-Zadeh, F., Wardle, M., Muno, M., Law, C., & Pound, M. 2005, Adv. Space Res., 35, 1074